

The *Swift* Bulge Survey: optical and near-IR follow-up featuring a likely symbiotic X-ray binary & a focused wind CV

A. W. Shaw,^{1,2★} C. O. Heinke,¹ T. J. Maccarone,³ G. R. Sivakoff,¹ J. Strader,⁴
 A. Bahramian,⁵ N. Degenaar,⁶ J. A. Kennea,⁷ E. Kuulkers,⁸ A. Rau,⁹
 L. E. Rivera Sandoval,³ L. Shishkovsky,⁴ S. J. Swihart,⁴ A. J. Tetarenko,¹⁰
 R. Wijnands,⁶ and J. J. M. in 't Zand¹¹

¹Department of Physics, University of Alberta, CCIS 4-181, Edmonton, AB T6G 2E1, Canada

²Department of Physics, University of Nevada, Reno, NV 89557, USA

³Department of Physics, Box 41051, Science Building, Texas Tech University, Lubbock, TX 79409-1051, USA

⁴Center for Data Intensive and Time Domain Astronomy, Department of Physics and Astronomy, Michigan State University, East Lansing, MI 48824, USA

⁵International Centre for Radio Astronomy Research-Curtin University, GPO Box U1987, Perth, WA 6845, Australia

⁶Anton Pannekoek Institute for Astronomy, University of Amsterdam, Postbus 94249, NL-1090 GE Amsterdam, the Netherlands

⁷Department of Astronomy and Astrophysics, The Pennsylvania State University, University Park, PA 16802, USA

⁸ESA/ESTEC, Keplerlaan 1, 2201, AZ Noordwijk, the Netherlands

⁹Max-Planck Institute for Extraterrestrial Physics, Giessenbachstr. 1, D-85748 Garching, Germany

¹⁰East Asian Observatory, 660 N. A'ohōkū Place, University Park, Hilo HI, USA, 96720

¹¹SRON Netherlands Institute for Space Research, Sorbonnelaan 2, NL-3584 CA Utrecht, the Netherlands

Accepted XXX. Received YYY; in original form ZZZ

ABSTRACT

The nature of very faint X-ray transients (VFXTs) – transient X-ray sources that peak at luminosities $L_X \lesssim 10^{36} \text{ erg s}^{-1}$ – is poorly understood. The faint and often short-lived outbursts make characterising VFXTs and their multi-wavelength counterparts difficult. In 2017 April we initiated the *Swift* Bulge Survey, a shallow X-ray survey of ~ 16 square degrees around the Galactic centre with the *Neil Gehrels Swift Observatory*. The survey has been designed to detect new and known VFXTs, with follow-up programmes arranged to study their multi-wavelength counterparts. Here we detail the optical and near-infrared follow-up of four sources detected in the first year of the *Swift* Bulge Survey. The known neutron star binary IGR J17445-2747 has a K4III donor, indicating a potential symbiotic X-ray binary nature and the first such source to show X-ray bursts. We also find one nearby M-dwarf (1SXPS J174215.0-291453) and one system without a clear near-IR counterpart (Swift J175233.9-290952). Finally, 3XMM J174417.2-293944 has a subgiant donor, an 8.7 d orbital period, and a likely white dwarf accretor; we argue that this is the first detection of a white dwarf accreting from a gravitationally focused wind. A key finding of our follow-up campaign is that binaries containing (sub)giant stars may make a substantial contribution to the VFXT population.

Key words: X-rays: binaries – infrared: stars – surveys – stars: neutron – binaries: symbiotic – novae, cataclysmic variables

1 INTRODUCTION

The majority of the brightest Galactic X-ray transients are binary systems in which a compact object, either a black

hole (BH) or a neutron star (NS), accretes matter from a stellar companion. Large variations in mass accretion rate cause their X-ray luminosities to increase by factors of $> 10^3$ and exceed $L_X \gtrsim 10^{36} \text{ erg s}^{-1}$ during outburst episodes, with a similar response at optical, near-infrared (NIR) and ultraviolet (UV) wavelengths (see e.g. Kuulkers 1998; Zurita

★ E-mail: aarrans@unr.edu

et al. 2006; Tucker et al. 2018). However, a fainter class of X-ray transients, very faint X-ray transients (VFXTs), display lower peak X-ray luminosities of $\sim 10^{34-36} \text{ erg s}^{-1}$ and corresponding faint optical/NIR outbursts (e.g. in 't Zand et al. 1999; Cornelisse et al. 2002; in 't Zand et al. 2005; Wijnands et al. 2006; Degenaar & Wijnands 2009; Armas Padilla et al. 2013; Shaw et al. 2018). Whilst classical X-ray transients are relatively well studied, the discovery and study of VFXTs has been hampered by sensitivity limitations of the X-ray, optical and NIR instruments that are best-suited to time domain work. Consequently the nature of VFXTs, and the cause of their sub-luminous outbursts, are not well understood.

Suggestions for the nature of VFXTs fall broadly into two groups: those with BH or NS accretors in some unusual state and other systems, often accreting white dwarf (WD) systems, such as intermediate polars (many of which reach $L_X > 10^{34} \text{ erg s}^{-1}$ and tend to be persistent, though some exhibit dwarf nova outbursts; Mukai 2017; Schwöpe 2018), novae (Mukai et al. 2008), and symbiotic stars (Luna et al. 2013; Mukai et al. 2016; Yungelson et al. 2019).

Explaining VFXTs as (NS or BH) X-ray binaries with unusual properties requires that the accretion flow, or its interaction with the compact object, be modified. The outburst-quiescence cycle of many disc-accreting compact objects can broadly be described by the disc instability model (DIM; see e.g. Lasota 2001, for a review). In this framework, accumulation of matter leads to the accretion disc reaching a critical temperature (the ionization temperature of the dominant species in the accretion disc), triggering a bright outburst due to the increased strength of the magneto-rotational instability in ionized gas relative to neutral gas, after which the disc cools as the source returns to quiescence. The DIM has been shown to reproduce the global behaviour of a number of transient and persistent low-mass X-ray binaries (LMXBs; e.g. Coriat et al. 2012; Tetarenko et al. 2016). However, it is difficult for the DIM to explain the faintness of VFXT outbursts, and their low time-averaged mass transfer rate, if they are produced by X-ray binaries similar to those that have been well-studied (Hameury & Lasota 2016).

The faintness of transient VFXT outbursts implies very small accretion discs, suggestive of short (e.g. $< 2 \text{ h}$) orbital periods (Shahbaz et al. 1998; King & Wijnands 2006; Heinke et al. 2015), interference with the flow of accreting matter onto the accretor, or that only a small part of a larger accretion disc is drained (Degenaar & Wijnands 2009).

The low time-averaged inferred mass transfer rates of VFXTs have inspired a range of possible explanations. It is possible that the true mass transfer rates from the donor are higher than we infer, implying accretion is hidden or that matter is thrown out before accreting onto the primary. Some VFXTs are known to be seen at high inclination (such that we are only viewing scattered X-rays; e.g. Munro et al. 2005b; Corral-Santana et al. 2013), but statistical arguments rule out this being the predominant VFXT mechanism (Wijnands et al. 2006). BH LMXBs at low mass transfer rates may be particularly faint, if their radiative efficiency continues to decline with luminosity (Maccarone & Patruno 2013; Kneivitt et al. 2014). Alternatively, mass transfer could be highly non-conservative (e.g. Hernández Santisteban et al. 2019). One scenario for quasi-persistent VFXTs (e.g. Heinke

et al. 2009, 2015) is that a strong magnetic field could impede the flow of matter onto the primary through a process known as the propeller effect (Illarionov & Sunyaev 1975). A rapidly rotating magnetic field in this case removes a large amount of the mass transferred from the companion, whilst some material may be able to reach the NS poles (Romanova et al. 2005), resulting in an overall low accretion rate. The identification of three “transitional” (switching between X-ray active and radio pulsar states) millisecond pulsars, which appear to accrete¹ quasi-persistently at $L_X \sim 10^{33-34} \text{ erg s}^{-1}$ (Papitto et al. 2013; Bogdanov et al. 2015; de Martino et al. 2013) shows that this is a plausible theory for other VFXTs.

Alternatively, the observed low mass transfer rates could reflect the real mass transfer rates from the donor. King & Wijnands (2006) suggested that mass transfer rates in VFXTs were so low as to require truly extreme scenarios, such as 100-1000 M_\odot BH accretors. Several authors have suggested accretion from the wind of a main-sequence (or subgiant) donor star (Bleach 2002; Pfahl et al. 2002; Maccarone & Patruno 2013). However, Heinke et al. (2015) showed that the low mass transfer rates seen in the Galactic Centre VFXTs can be explained by standard binary evolution involving either normal H-rich donors, or H-poor (white dwarf) donors, in either case culminating in $\ll 0.1 M_\odot$, partly degenerate donor stars in $\sim 2 \text{ h}$, or $\sim 90 \text{ min}$ (respectively), orbits. On the other hand, it is clear that these short-orbit systems cannot make up most VFXTs, based on evidence from several VFXT optical/infrared counterparts (Degenaar et al. 2010; Shaw et al. 2017a).

To develop a complete understanding of VFXTs we require dedicated multi-wavelength studies of a substantial population. In particular, the companion stars of X-ray binaries are usually only accessible through optical/NIR follow-up of sources discovered in X-ray surveys. Furthermore, it is well-established that VFXTs represent a heterogeneous class of systems, and that an extensive survey is necessary to unveil the relative proportions of different mechanisms.

2 THE SWIFT BULGE SURVEY

The majority of VFXTs so far discovered have been found through frequent monitoring of the dense region around the Galactic Centre (Munro et al. 2005a; Wijnands et al. 2006; Degenaar & Wijnands 2009, 2010; Degenaar et al. 2012). However, the Galactic Centre is inaccessible to optical and infrared follow-up of typical X-ray binary companions, due to its extreme extinction and stellar crowding (Bandyopadhyay et al. 2005; Laycock et al. 2005; DeWitt et al. 2010). We therefore planned a survey designed to repeatedly monitor a large swath of the Galactic Bulge, much of which experiences low enough reddening and stellar crowding to enable plausible optical/infrared follow-up. To this end, in 2017 April we initiated the *Swift* Bulge Survey (SBS; see e.g. Heinke et al. 2017; Bahramian et al. 2017), a shallow (60 s exposures) monitoring campaign of ~ 16 square degrees around the Galactic Centre with the *Neil*

¹ (or possibly stimulate enhanced radio pulsar activity; see Ambrosino et al. 2017)

Gehrels Swift Observatory/X-ray Telescope and Ultraviolet/Optical Telescope (*Swift*/XRT and *Swift*/UVOT; Burrows et al. 2005; Roming et al. 2005), designed to detect new and known VFXTs and study X-ray variability in the direction of the Galactic Bulge in the low flux regime (see Bahramian et al. 2020, in prep., for details). In the first year of this survey 2017 April – 2018 March), we obtained a total of 19 biweekly epochs. In addition to the SBS observations, we also obtained target of opportunity (ToO) triggers with a multitude of optical, NIR, radio and X-ray facilities to follow up sources detected in the X-ray survey in an effort to derive the natures of such sources. The details of the X-ray survey are described by Bahramian et al. (2020, in prep.) and the UV results are presented by Rivera Sandoval et al. (2020, in prep.). In this work we describe the results from our optical/NIR follow-up campaign, the targets of which are as follows: previously known sources **IGR J17445–2747**, **1SXPS J174215.0–291453** and **3XMM J174417.2–293944** and the newly discovered source **Swift J175233.9–290952**. The targets are described in more detail in Appendix A (see also Bahramian et al. 2020, in prep.).

In Section 3 we describe the follow-up observations we have utilized in this work. In Section 4 we present our analysis techniques and the results from the observational data. We discuss the implications in Section 5 and provide a summary in Section 6.

3 OBSERVATIONS AND DATA REDUCTION

We used several optical and NIR facilities to follow up X-ray sources detected in the SBS. We detail here the follow-up observations and the steps we took to reduce and calibrate the data. We summarise our follow-up observations in Table 1.

3.1 NIR photometry

We obtained NIR images of the IGR J17445–2747 field on 2017 April 18 with the Near InfraRed Imager and spectrograph (NIRI) on the 8.1m *Gemini* North telescope at Mauna Kea, Hawaii as part of proposal GN-2017A-Q-259 (PI: Bahramian). The instrument was operating in imaging mode with the f/6 camera. We obtained 10 exposures of 27.5 s in the *J*, *H* and *K* broad-band filters. To account for the changing sky background at NIR wavelengths, a dithering pattern was applied in each filter, with each co-added exposure consisting of 25 exposures of 1.1s.

To reduce the data we used the Image Reduction and Analysis Facility (IRAF; Tody 1986) *Gemini* package, in conjunction with NIRI-specific PYTHON routines. We utilized the `cleanir` script² to remove artifacts superimposed by the IR detector controller, and corrected for non-linearity in the detector with `nirlin`.³ Sky frames were created from the science images, as there were no extended objects in the field. For each target, a normalized flat-field was created with the task `niflat` and bad pixels identified using short dark

frames. Flat-fielding and sky subtraction was performed using `nireduce` and created final images with `imcoadd`.

To derive the correct astrometry we first used SEXTRACTOR (Bertin & Arnouts 1996) to create source catalogues for the images in each band. The astrometric solution was calculated with SCAMP (Bertin 2006) using 2MASS as a reference, providing a typical astrometric accuracy of 0''.01 in both RA and Dec. The astrometric solution was then mapped to the co-added images with SWARP (Bertin et al. 2002).

We utilized the IRAF DAOPHOT routines developed for crowded field photometry (Stetson 1987). We determined the empirical point spread function (PSF) for each target frame using 15 relatively isolated field stars present in the UKIDSS catalogue. Using the fitted PSF, we subtracted close neighbors of the UKIDSS stars from the images, and used these (now isolated) stars to calibrate the photometry. We performed aperture photometry on both the target and the calibration stars with the task `phot`, employing a 10 pixel (1''.16) radius circular aperture for the target and a 15 pixel (1''.75) radius for the calibration stars. The appropriate aperture correction was computed with the task `mkapfile`. To convert between instrumental magnitudes and the UKIDSS magnitude system we used the IRAF task `fitparams` and transformation equations of the form

$$j = J + c_1 + c_2 X_j + c_3 (J - H), \quad (1)$$

$$h = H + c_4 + c_5 X_h + c_6 (H - K), \quad (2)$$

$$k = K + c_7 + c_8 X_k + c_9 (H - K), \quad (3)$$

where, *j*, *h*, *k* are the instrumental magnitudes in the appropriate filter, *J*, *H*, *K* are the known magnitudes of the calibration stars, *c*_{1–9} are constants (representing an additive term, an extinction term and a colour term in each band) and *X*_{*j,h,k*} are the average airmasses for observations in each band. We estimate uncertainties on the measured magnitudes of the target by calculating the root-mean-square (RMS) error, comparing the catalogue magnitudes of the calibration stars with those derived by our photometry.

We obtained NIR imaging observations of the Swift J175233.9–290952 field on 2017 May 9 with the Gamma-Ray Burst Optical/Near-Infrared Detector (GROND; Greiner et al. 2008, PI: Rau) mounted on the 2.2m MPI/ESO telescope at La Silla, Chile. We obtained simultaneous imaging in the *J*, *H*, and *K*-bands, consisting of 56, 10 s exposures in each of *J* and *K* and 48, 10 s exposures in *H*. Data were reduced and photometry was performed with the GROND manual analysis pipeline v2.2, which used 2MASS stars in the field to derive the astrometric solution, achieving an astrometric accuracy of 0''.03 or better in each band. Instrumental magnitudes were calibrated on to the 2MASS photometric system using the known NIR transformations (Greiner et al. 2008).

3.2 NIR spectroscopy

On 2017 June 26 we obtained spectroscopy of the region surrounding the *Chandra* position of Swift J175233.9–290952

² <http://staff.gemini.edu/~astephens/niri/cleanir/cleanir.py>

³ <http://staff.gemini.edu/~astephens/niri/nirlin>

Table 1. Summary of optical/NIR observations of sources detected in the SBS that we utilized in this work. For each X-ray source we also give the coordinates, positional uncertainty and the name of the X-ray observatory that constrained the position.

IGR J17445–2747 $17^{\text{h}}44^{\text{m}}30^{\text{s}}.437$ $-27^{\circ}46'00''.32$ ($1''$; <i>Chandra</i>)			
Date	Telescope/Instrument	Filter/Grating	Exposure Time
2017 April 18	<i>Gemini</i> /NIRI	<i>J</i> , <i>H</i> , <i>K_s</i>	275 s, 275 s, 275 s
2017 April 24	<i>SOAR</i> /Goodman	400 l mm ⁻¹	1800 s
2018 May 09	<i>Gemini</i> /Flamingos-2	R3K <i>J</i> , <i>K_s</i>	1200 s, 600 s
Swift J175233.9–290952 $17^{\text{h}}52^{\text{m}}33^{\text{s}}.934$ $-29^{\circ}09'47''.92$ ($0''.7$; <i>Chandra</i>)			
Date	Telescope/Instrument	Filter/Grating	Exposure Time
2017 May 9	MPI/ESO 2.2m/GROND	<i>J</i> , <i>H</i> , <i>K</i>	560 s, 480 s, 560 s
2017 June 26	<i>VLT</i> /SINFONI	<i>H</i> + <i>K</i>	4560 s
1SXPS J174215.0–291453 $17^{\text{h}}42^{\text{m}}14^{\text{s}}.995$ $-29^{\circ}14'59''.40$ ($0''.4$; <i>XMM-Newton</i>)			
Date	Telescope/Instrument	Filter/Grating	Exposure Time
2016 March 10 – 2018 September 23	ASAS-SN	<i>V</i>	90 s (per exposure)
2017 May 28	<i>SOAR</i> /Goodman	400 l mm ⁻¹	300 s
3XMM J174417.2–293944 $17^{\text{h}}44^{\text{m}}17^{\text{s}}.246$ $-29^{\circ}39'44''.31$ ($0''.5$; <i>XMM-Newton</i>)			
Date	Telescope/Instrument	Filter/Grating	Exposure Time
2016 March 10 – 2018 September 23	ASAS-SN	<i>V</i>	90 s (per exposure)
2017 September 29	<i>VLT</i> /SINFONI	<i>H</i> + <i>K</i>	1280 s
2018 March 25 – September 15	<i>SOAR</i> /Goodman	2100 l mm ⁻¹	600 s (per night) ^a

^a Typical setup, see text for further details and exceptions

with the Spectrograph for INtegral Field Observations in the Near Infrared (SINFONI; Eisenhauer et al. 2003) integral field unit (IFU) on the *Very Large Telescope* (*VLT*) at Paranal, Chile. Target of Opportunity (ToO) observations were obtained as part of proposal 099.D-0826 (PI: Dege-naar). We obtained 19 images, each a co-add of 4 dithered 60 s exposures (to account for the variable NIR sky background), using the *H* + *K* grating. We utilized the $0''.25$ pixel scale, which provides a typical full width at half maximum (FWHM) resolution of 11.8 \AA . We used a nearby $R = 13.7$ star as a natural guide star (NGS) to correct for atmospheric distortions with the SINFONI adaptive optics (AO).

Data were reduced using the ESO Recipe Execution tool (ESOREX) pipeline⁴, which performs typical reduction steps including dark subtraction, non-linearity correction, flat fielding and wavelength calibration to provide a co-added data cube. The astrometric solution for the median image was derived with the IRAF task *ccmap*, using 6 UKIDSS stars in the small FOV image. The solution provided an accuracy of $0''.03$ and $0''.01$ in RA and Dec, respectively. We extracted the spectrum of the suspected counterpart with the ESOEX task *sinfo_utl_cube2spectrum*, using a circular region with a 3 pixel ($0''.375$) radius.

To correct for (terrestrial) telluric features of the *VLT* spectra we used MOLECFIT (Smette et al. 2015; Kausch, W. et al. 2015), which fits a number of telluric lines in the science spectrum to derive a telluric transmission spectrum for the entire spectral range. This spectrum is then divided through the science spectrum, resulting in a spectrum rel-

atively free of telluric absorption. MOLECFIT is able to use the science spectrum as an input, rather than a telluric standard, meaning that the transmission spectrum we derive is representative of the NIR sky spectrum under the actual observing conditions, as opposed to telluric standard stars observed at different times, airmasses, and sky conditions.

We obtained IFU spectroscopy of the 3XMM J174417.2–293944 field with *VLT*/SINFONI on 2017 September 29. We obtained 32 images, each a co-add of 4 dithered 10 s exposures, using the *H*+*K* grating. We utilized the $0''.1$ spatial pixel scale, providing a typical FWHM resolution of 10 \AA . We used the target itself as the NGS for the AO correction. Data were reduced in the same manner as for Swift J175233.9–290952, using a circular region with a 6 pixel ($0''.3$) radius centred on the star. The spectrum was corrected for telluric features with MOLECFIT, ensuring that stellar lines were excluded from the fit.

On 2018 May 09 we obtained long slit spectroscopy of 2MASS J17443041–2746004, the suspected NIR counterpart to IGR J17445–2747 (Shaw et al. 2017b), with Flamingos-2 on the 8.1m *Gemini* South telescope at Cerro Pácon, Chile, as part of the poor weather proposal GS-2018A-Q-407 (PI: Shaw). We obtained 2x600 s exposures in the *J*-band and 2x300 s exposures in the *K_s*-band, utilising the R3K disperser in both instances, providing a typical FWHM resolution of 4 \AA in the *J*-band and 7 \AA in the *K_s*-band. The second exposure in each band was offset along the two pixel ($0''.36$) wide slit by $10''$ to aid sky subtraction by accounting for the changing sky background at NIR wavelengths. We also obtained 4x30 s observations of the telluric standard A0V star HD 155379 in each band.

Data were reduced using the IRAF *Gemini* package.

⁴ <https://www.eso.org/sci/software/cpl/esorex.html>

Flat fielding and dark subtraction was performed with the task `nsreduce`. The wavelength solution was obtained with `nswavelength` and applied to all telluric and science frames before spectra were extracted with `nsextract`. We normalised the averaged spectrum of the telluric standard and removed the hydrogen absorption features at Brackett γ (Br γ ; 2.166 μm) and Paschen β (Pa β ; 1.282 μm) with a best-fit Voigt profile. We then used the IRAF task `telluric`, which shifts and scales the science and telluric spectra to best divide out telluric features from the science spectra.

3.3 Optical Spectroscopy

On 2017 April 24 we obtained a single 1800 s spectrum of *Gaia* DR2 4060626256817246720, the faint ($i \sim 19.4$) optical counterpart consistent with the *Chandra* position of IGR J17445–2747, with the Goodman Spectrograph (Clemens et al. 2004) on the 4.1m *SOuthern Astrophysical Research (SOAR)* telescope, on Cerro Pachón, Chile (PI: Strader). We used a $0''.95$ slit and a 400 line mm^{-1} grating, with an approximate wavelength coverage of $\sim 4800\text{--}8800$ Å at a FWHM resolution of 5.6 Å. The 1D spectrum was optimally extracted from the 2D CCD image using the IRAF task `apall`. The target spectrum was wavelength calibrated using the task `identify` and a single spectrum of the FeAr lamp. Flux calibration of the target spectrum was performed using the flux standard star CD-32 9927.

On 2017 May 28 we obtained a single 300 s spectrum of *Gaia* DR2 4057126472597377152, the optical counterpart to 1SXPS J174215.0–291453, with *SOAR*/Goodman. We used an identical setup to the *SOAR*/Goodman observations of IGR J17445–2747, and reduction was carried out in the same manner, including using the same flux standard star.

We obtained spectra of *Gaia* DR2 4057051396569058432, the optical counterpart to 3XMM J174417.2–293944, with *SOAR*/Goodman over 17 epochs from 2018 Mar 25 to 2018 Sep 15 UTC. At each epoch we obtained two (typically 300 s) spectra back to back. Most observations used a 2100 line mm^{-1} grating and a $0''.95$ slit, yielding a resolution of 0.8 Å FWHM over $\sim 6030\text{--}6615$ Å. On 2018 Aug 25, we instead used a narrower $0''.45$ slit to yield an improved resolution of 0.5 Å. On 2018 Aug 13 only a 1200 line mm^{-1} grating was available, which gave a lower resolution of 1.7 Å. All spectra were reduced and optimally extracted in the same manner as IGR J17445–2747 and 1SXPS J174215.0–291453. To compute radial velocities (RVs), we also observed a K giant with the same setup.

3.4 Long-term Optical Monitoring

The optical counterparts to 1SXPS J174215.0–291453 and 3XMM J174417.2–293944 are monitored in the *V*-band by the All-Sky Automated Survey for Supernovae (ASAS-SN; Shappee et al. 2014; Kochanek et al. 2017). We generated and downloaded light curves for each counterpart using the web interface⁵, using a $16''$ aperture centred on the source position, which is calibrated against the American Association of Variable Star Observers (AAVSO) Photometric

⁵ <https://asas-sn.osu.edu>

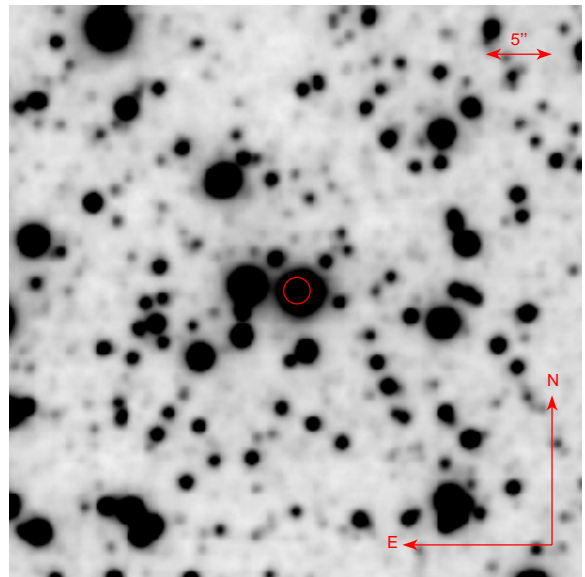


Figure 1. *Gemini*/NIRI *K*-band image of the IGR J17445–2747 field. The red circle represents the $1''$ radius error circle of the *Chandra* X-ray position of the source (Chakrabarty et al. 2017)

All-Sky Survey (APASS; Henden et al. 2012). *V*-band photometry for both sources spans the range 2016 March 10 – 2018 September 23 and comprises ~ 750 measurements with an average cadence of ~ 1.25 d.

4 ANALYSIS AND RESULTS

4.1 IGR J17445–2747

4.1.1 NIR Photometry

Fig. 1 shows the *Gemini*/NIRI *K*-band image of the IGR J17445–2747 field. The *Chandra* X-ray position is consistent with a bright source from the Two Micron All Sky Survey (2MASS; Skrutskie et al. 2006) catalogue, 2MASS J17443041–746004, with magnitudes of $J = 12.53 \pm 0.06$, $H = 10.45 \pm 0.06$ and $K_s = 9.65 \pm 0.06$. We measure $J = 12.55 \pm 0.08$, $H = 10.61 \pm 0.14$ and $K = 9.69 \pm 0.07$ in our NIRI images. We found no evidence for any new outbursting source within the *Chandra* error circle. The star’s PSF is Gaussian, suggesting it is not confused.

Our NIRI magnitudes are completely consistent with those of the 2MASS catalogue. However, a lack of variability does not rule it out as the true NIR counterpart of IGR J17445–2747. It is possible that the source had decayed to NIR quiescence at the time of the NIRI observations, as they were performed five days after the detection of the X-ray outburst by *Swift*. However, the source was still detected in X-rays (at a 0.3–10 keV unabsorbed flux $F_X \sim 2 \times 10^{-11} \text{ erg s}^{-1} \text{ cm}^{-2}$) at the time of the NIRI observations (Bahramian et al. 2020, in prep.).

We calculate the probability that 2MASS J17443041–746004 is a chance alignment with the *Chandra* position to be just 0.3 per cent. We calculate this by considering the $1''$ uncertainty on the *Chandra* position of the X-ray source (Chakrabarty et al. 2017) and the spatial density of NIR sources as bright or brighter

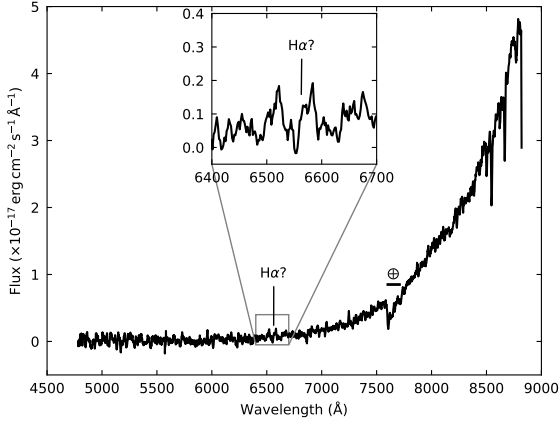


Figure 2. *SOAR/Goodman* spectrum of the suspected optical counterpart to IGR J17445–2747, smoothed with a 5-point boxcar function. A zoomed in portion of the region around 6562.8 Å is shown inset, indicating a potential weak H α emission feature. The absorption feature at 7590–7720 Å is due to atmospheric absorption in the O $_2$ A-band and is labelled with the \oplus symbol.

than 2MASS J17443041–746004 (91 such sources in a 3' radius around the X-ray position). We note that if we consider NIR sources that are at least 1 per cent the flux of 2MASS J17443041–746004, this probability is still as low as 3 per cent. It is therefore highly likely that this bright source is the true counterpart to IGR J17445–2747.

4.1.2 Optical Spectroscopy

The *SOAR/Goodman* spectrum of the suspected optical counterpart to IGR J17445–2747 is shown in Fig. 2. The spectrum suffers from heavy extinction, with the source barely detected above the noise at wavelengths $\lesssim 7000$ Å in the 1800 s exposure. Considering the source is extremely bright at NIR wavelengths, its faintness in the optical regime suggests that the source is likely not a close-by dwarf star.

Highlighted in Fig. 2 is a possible emission feature that could be consistent with H α and therefore an indication of an accreting system. However, as the supposed feature is located in a region of the spectrum where pixel-to-pixel noise variations dominate, we cannot confirm its identity as a true emission line. We must instead focus on the properties of the NIR spectrum to interpret the nature of the system.

4.1.3 NIR Spectroscopy

The *J*- and *K_s*-band *Gemini/Flamingos-2* spectra of 2MASS J17443041–746004, the suspected NIR counterpart to IGR J17445–2747, are shown in Fig. 3. We identified a number of prominent lines in the spectra and used the `rvid-lines` IRAF task to measure the radial velocity (RV) of the source, deriving a heliocentric velocity $v_{\text{helio}} = 208 \pm 27 \text{ km s}^{-1}$ and $v_{\text{helio}} = 208 \pm 13 \text{ km s}^{-1}$ in the *J*- and *K_s*-band spectra, respectively. These velocities were applied to the relevant spectra, resulting in the Doppler corrected versions plotted in Fig. 3. We identified spectral lines using published spectral libraries for late-type stars (Kleinmann & Hall 1986;

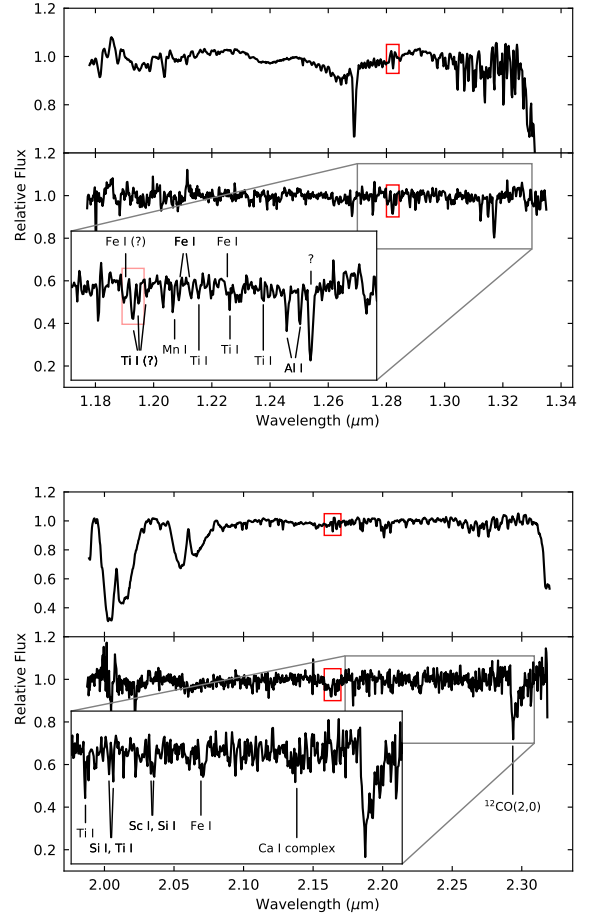


Figure 3. *Gemini/Flamingos-2* spectra of 2MASS J17443041–746004, the suspected NIR counterpart to IGR J17445–2747, with the *J*-band in the *top* and *K_s*-band in the *bottom* sub-figures. In both sub-figures, the upper panel shows the telluric transmission spectrum used to correct the target spectrum and the lower panel continuum normalised, telluric corrected spectrum of the target, velocity corrected to the rest frame using the heliocentric velocity $v_{\text{helio}} = 208 \text{ km s}^{-1}$. In both sub-figures we show a zoomed in portion of the target spectrum, with some spectral lines identified and labelled. The red boxes highlight where hydrogen lines (Pa β in the *J*-band and Br γ in the *K_s*-band) have been removed from the spectrum of the telluric standard, resulting in some residuals that may have affected the telluric correction. As such, any line identifications in this region are labelled as uncertain with ‘(?)’. The line labeled ‘?’ in the *J*-band spectrum is an unknown absorption feature.

Wallace & Hinkle 1997; Wallace et al. 2000) and the National Institute of Standards and Technology - Atomic Spectra Database (NIST-ASD; Kramida et al. 2018).

The most prominent lines in the NIR spectrum are neutral metal species (e.g. Al I, Ti I) and the molecular ^{12}CO (2,0) bandhead, typically associated with late-type (K–M) stars (see e.g. Kleinmann & Hall 1986; Wallace & Hinkle 1997; Wallace et al. 2000). The strong ^{12}CO feature, combined with the brightness of the NIR counterpart and faintness of the optical counterpart provide compelling evidence that the optical/NIR counterpart is a distant late-type giant. We see no evidence for Pa β or Br γ emission.

Table 2. Definitions of the spectral features and the passbands used to estimate the continuum at each feature for two-dimensional spectral classification. We use the same definitions as Bahramian et al. (2014).

Feature	Line		Blue continuum		Red continuum	
	Centre (μm)	$\delta\lambda$	Centre (μm)	$\delta\lambda$	Centre (μm)	$\delta\lambda$
Na I	2.2075	0.007	2.1940	0.006	2.2150	0.004
Ca I	2.2635	0.011	2.2507	0.0106	2.2710	0.002
^{12}CO	2.2955	0.013	2.2500	0.016	2.2875	0.007

Table 3. Equivalent widths of spectral features in the *Gemini*/Flamingos-2 K_s -band spectrum of the NIR counterpart to IGR J17445–2747

Feature	EW (\AA)
Na I	1.21 ± 0.27
Ca I	0.66 ± 0.95
^{12}CO	13.50 ± 0.88

We test the giant hypothesis by adopting the approach of Bahramian et al. (2014) and applying two-dimensional spectral classification techniques to the K_s -band spectrum of IGR J17445–2747. These techniques follow the methods of Ramirez et al. (1997); Ivanov et al. (2004) and Comerón et al. (2004), who identify spectral features that are temperature dependent and compare them with features that are both temperature and surface gravity dependent. We adopt the Na I and Ca I passbands centred at 2.2075 and 2.2635 μm , respectively, as the temperature dependent features, and the ^{12}CO (2,0) bandhead centred at 2.2955 μm as the temperature and surface gravity dependent feature. For each feature we calculate the equivalent width (EW), approximating the continuum level with a best-fit 1-dimensional polynomial (ASTROPY’s `Polynomial1D`) using two nearby, featureless regions of the spectrum. We use the same feature and continuum definitions as Bahramian et al. (2014), who follow the method of Comerón et al. (2004, see Table 2).

We estimated uncertainties on the reported EWs using the ‘bootstrap-with-replacement’ technique. We determined 10000 new EWs using continuum levels from a random sample of the passbands described in Table 2 and computed the standard error. For each new continuum passband, we allowed the same wavelength-flux pair to be selected multiple times (hence ‘replacement’). The EWs and uncertainties are reported in Table 3, and discussed in Section 5.1.

4.2 Swift J175233.9–290952

4.2.1 NIR imaging

Fig. 4 shows the GROND K -band image of the Swift J175233.9–290952 field. There is no source detected inside the *Chandra* error circle. The 3σ limiting magnitudes of the GROND images are $K < 14.6$, $H < 14.8$ and $J < 15.8$. The proposed counterpart, VVV J175233.93–90947.66, has $J = 16.4 \pm 0.1$ and $H = 15.1 \pm 0.1$, so had not brightened significantly at the time of the GROND observations, five days after the initial Swift detection. The source was still X-ray active at the time of the GROND observations (Bahramian et al. 2020, in prep.) but it is possible that a NIR outburst could have decayed by this point.

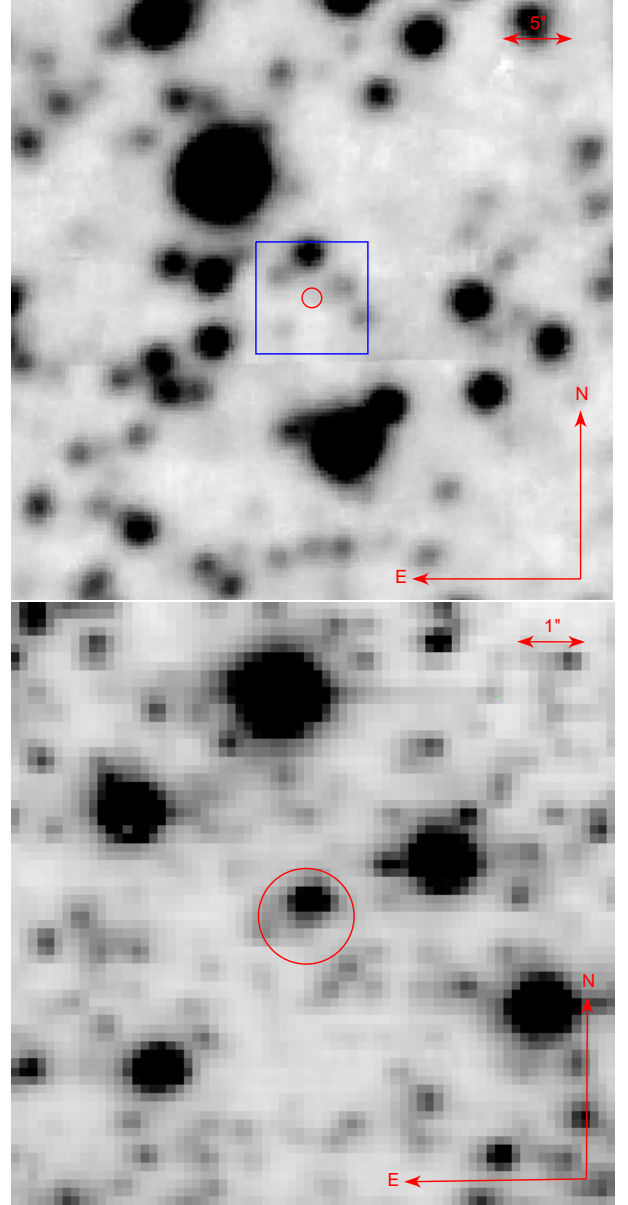


Figure 4. Images of the Swift J175233.9–290952 field. The top sub-figure shows GROND K -band image, observed five days after the detection of the X-ray source. The blue box represents the approximate FOV of the VLT/SINFONI spectroscopic follow-up, the median cube image (the full data cube compressed on the spectral axis) of which is shown in the bottom sub-figure. In both sub-figures the red circle represents the $0.7''$ radius error circle of the *Chandra* X-ray position of the source.

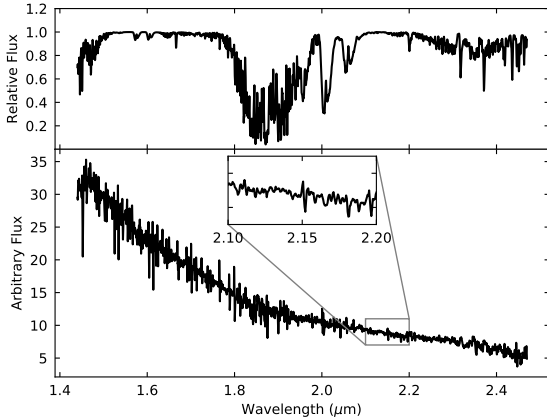


Figure 5. VLT/SINFONI *H+K*-band spectrum of VVV J175233.93–90947.66, the suspected NIR counterpart to Swift J175233.9–290952. The upper panel shows the telluric transmission spectrum derived with MOLECFIT and used to correct the target spectrum. The lower panel shows the telluric corrected spectrum of the target and has not been continuum normalised. The lower panel inset shows a zoomed in portion of the target spectrum around the rest wavelength of Br γ , highlighting the absence of emission features in this spectral region.

4.2.2 NIR spectroscopy

The VLT/SINFONI median cube image of the Swift J175233.9–290952 field, obtained 49 d after the GROND imaging observation, is also shown in Fig. 4 and shows the suspected counterpart, VVV J175233.93–90947.66, in the *Chandra* error circle. We calculate a chance alignment probability of 8 per cent. We studied the VVV light curve of this source⁶ to search for outbursting behaviour or other variability, which may help us identify it as the correct counterpart. However, aside from an apparent ~ 1 magnitude drop at MJD ~ 55309 that is likely poor calibration (as the same pattern appears in comparison stars), there was no variability.

The spectrum of VVV J175233.93–90947.66, shown in Fig. 5, is strikingly featureless and dominated by noise (particularly in the *H*-band), with no evidence for hydrogen emission at Br γ , or any other features common in accreting binaries. There are also no absorption features suggestive of a late-type star (e.g. CO bandheads), which, with the lack of an optical counterpart, rules out a close-by flaring dwarf.

A second, fainter source lies partially inside the *Chandra* error circle in Fig. 4, which is not present in any NIR source catalogues, making the identification of the true counterpart less certain. Through comparison with the catalogued sources in the image, we estimate $K \sim 18$ for the fainter source. We extract a low S/N spectrum, to search for strong accretion signatures, but do not find any evidence of Br γ . With the two possible counterparts in mind, we discuss the nature of Swift J175233.9–290952 in Section 5.2.

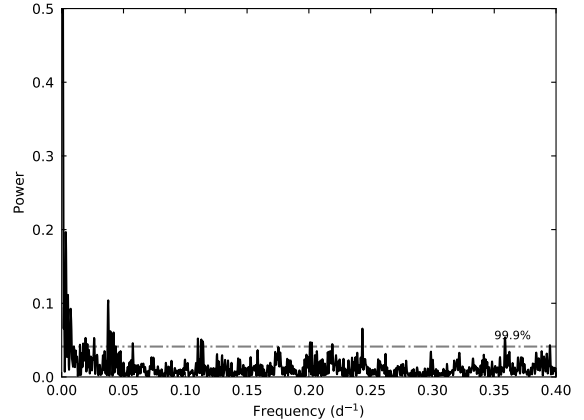


Figure 6. Lomb-Scargle periodogram, calculated using the ASAS-SN *V*-band photometry of the optical counterpart to 1SXPS J174215.0–291453. The dash-dotted line represents the 99.9 per cent significance power.

4.3 1SXPS J174215.0–291453

4.3.1 Long-term Optical Monitoring

ASAS-SN has monitored *Gaia* DR24057126472597377152 (*Gaia* Collaboration et al. 2016, 2018), the optical counterpart to 1SXPS J174215.0–291453, for ~ 2.5 y. We performed timing analysis on the *V*-band light curve to search for periodicities, P , that may identify a binary orbital period (P_{orb}). Periodicities are determined using a Lomb-Scargle periodogram analysis (Lomb 1976; Scargle 1982), which utilizes least-squares fitting of sinusoids to the light curve data to determine the power at each frequency. Lomb-Scargle analysis was performed using ASTROPY (Astropy Collaboration et al. 2013, 2018).

The periodogram is shown in Fig. 6. The significance of the power (represented in Fig. 6 by a dash-dotted line at 99.9 per cent confidence) is calculated by randomly shuffling the light curve magnitudes but keeping the time-stamps the same, in essence creating a randomized light curve but with the same sampling as the original data. This algorithm is excellent for identifying the peaks which are significant relative to a white noise power spectrum, but it can identify apparently significant peaks which are not significant relative to a red noise power spectrum; where statistically significant variability is detected, it is likely to be real variability, but further work must be done to determine whether the variability is periodic or aperiodic. The peak Lomb-Scargle powers were recorded for 10000 of the random light curves and the significance percentiles derived. The highest peak suggests a periodicity of $P = 926$ d, which is the length of the light curve, so simply indicates a long-term brightening trend. over the course of the ASAS-SN monitoring. There are other peaks above the 99.9 per cent confidence level, but folding the light curves on these periods reveals no periodic structure, and so it is likely that these peaks are indicating red noise rather than periodic variability. We do not consider 1SXPS J174215.0–291453 to exhibit a periodicity.

⁶ generated from the detection table at the source position, http://horus.roe.ac.uk:8080/vdfs/Vregion_form.jsp

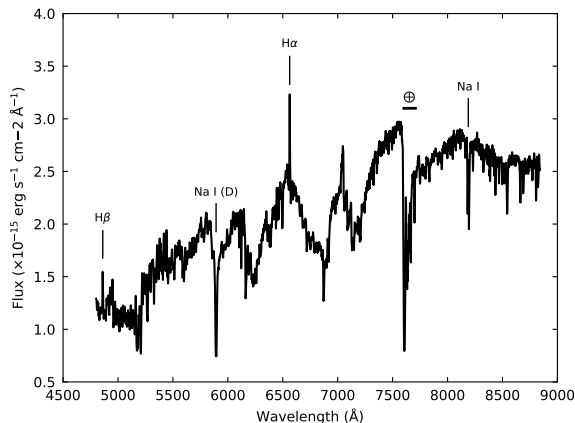


Figure 7. *SOAR/Goodman* spectrum of *Gaia* DR2 4057126472597377152, the optical counterpart to 1SXPS J174215.0–291453 (=3XMM J174214.9–9145), velocity corrected to the rest frame using the heliocentric velocity $v_{\text{helio}} = -104 \pm 2 \text{ km s}^{-1}$. Some spectral lines have been identified and labelled. The absorption feature at 7590–7720 Å is due to atmospheric absorption in the O₂ A-band and is labelled with the \oplus symbol.

4.3.2 Optical Spectroscopy

The *SOAR/Goodman* spectrum of *Gaia* DR2 4057126472597377152 is shown in Fig. 7. There are a number of strong absorption lines in the optical spectrum, in particular Na I, which is intrinsic to late-type stars and likely contributes to the interstellar Na D doublet at 5890 Å and 5896 Å. In addition, the broad absorption bandheads in the range ~ 6100 – 7400 Å are likely due to a combination of CaH, CaOH and TiO, common in late-type (late K–M) stars (Reid et al. 1995; Hawley et al. 1996).

We also identified narrow Balmer emission lines, and used these along with the IRAF task `rvidlines` to measure the RV of the source, deriving a heliocentric velocity $v_{\text{helio}} = -104 \pm 2 \text{ km s}^{-1}$. This velocity was applied to the spectrum, resulting in the Doppler corrected version plotted in Fig. 7.

We can use the optical spectrum to derive the spectral type of 1SXPS J174215.0–291453, similarly to IGR J17445–2747. Reid et al. (1995) defined a series of flux ratios to measure the molecular features in late-type stellar spectra. The ratio is defined as $R = F_{\text{W}}/F_{\text{cont}}$, where F_{W} is the integrated flux of the feature, normalised by the bandwidth, and F_{cont} is a pseudo-continuum flux, ie. the mean flux in a defined sideband. The strongest TiO bandhead (TiO 5; 7126–7135 Å) serves as the most reliable spectral type indicator between K7 and M6.5, and using the range 7042–7046 Å to calculate F_{cont} we find $R \approx 0.67$. We discuss the implications in Section 5.3.

4.4 3XMM J174417.2–293944

4.4.1 Long-term Optical Monitoring

ASAS-SN has monitored the optical counterpart to 3XMM J174417.2–293944 for ~ 2.5 y. We performed a Lomb-

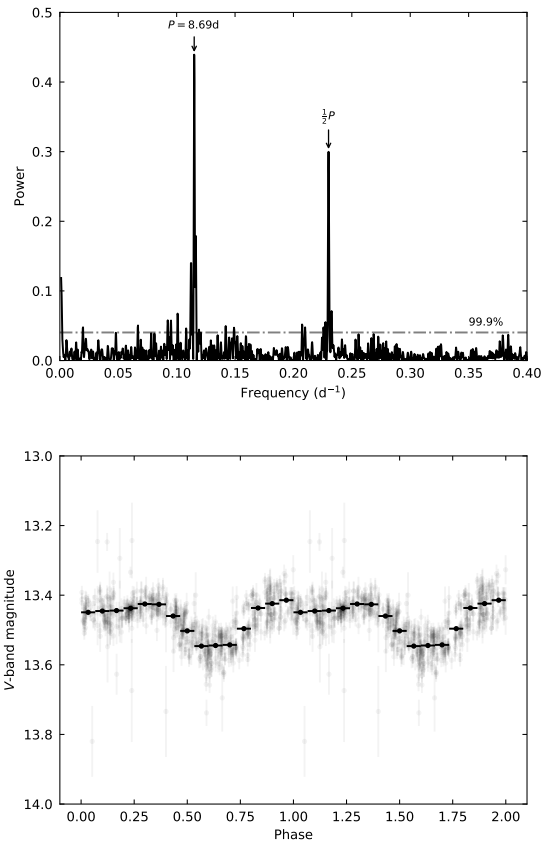


Figure 8. Timing analysis of the long-term V-band monitoring of the optical counterpart to 3XMM J174417.2–293944 with ASAS-SN. The *top* sub-figure shows the Lomb-Scargle periodogram. The periodicity, P , implied by the peak power is labeled along with its $\frac{1}{2}P$ alias. The dash-dotted line represents the 99.9 per cent significance power. The *bottom* sub-figure shows the ASAS-SN V-band light curve folded on the periodicity $P = 8.69$ d inferred from the periodogram. The grey points represent the unbinned folded light curve; black points are grouped into 15 bins per cycle.

Scargle periodogram analysis on the V-band light curve to search for signatures of a potential P_{orb} .

The periodogram is shown in Fig. 8, highlighting the peak power at $P = 8.69 \pm 0.05$ d, consistent with the period reported by ASAS-SN⁷ and, as we later report in Section 4.4.3, the P_{orb} derived from the RV study. The uncertainty on P was determined with the ‘bootstrap-with-replacement’ technique, whereby the light curve is reconstructed using a random sample of the original ASAS-SN light curve, allowing each time-flux pair to be selected multiple times. 10000 of these light curves are subjected to Lomb-Scargle periodogram analysis and the standard deviation of the peak periodicities are used to determine the uncertainty on P . The significance of the power was calculated in the same way as for 1SXPS J174215.0–291453.

The ASAS-SN V-band lightcurve, folded on the optimal period $P = 8.69$ d implied by the Lomb Scargle analysis, is also presented in Fig. 8. We choose the reference time $T_0 = 2458334.9450$ (BJD), derived from the RV study (see

⁷ <https://asas-sn.osu.edu/variables/230506>

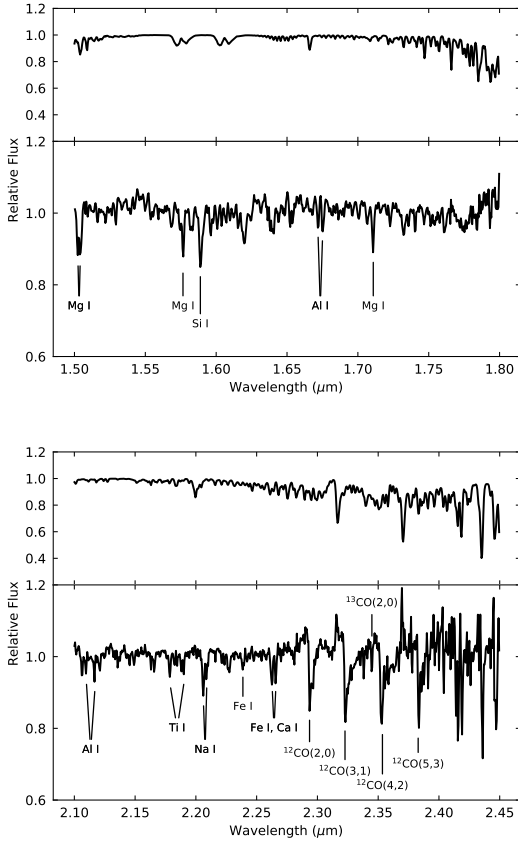


Figure 9. VLT/SINFONI spectra of the NIR counterpart to 3XMM J174417.2–293944 with the *H*-band portion of the spectrum in the *top* and *K*-band portion of the spectrum in the *bottom* sub-figure. In both sub-figures, the upper panel shows the telluric transmission spectrum derived with MOLECFIT and used to correct the target spectrum and the lower panel shows the continuum normalised, telluric corrected spectrum of the target. The *H*-band spectrum has been velocity corrected to the rest frame using the heliocentric velocity $v_{\text{helio}} = 134 \pm 7 \text{ km s}^{-1}$ and the *K*-band spectrum corrected using $v_{\text{helio}} = 45 \pm 7 \text{ km s}^{-1}$. Some spectral lines have been identified and labelled in the lower panel of each sub-figure.

Section 4.4.3) when constructing the folded light curve so we can directly compare to the RV curve. The folded light curve shows a distinct modulation, reminiscent of orbital variability seen in binary systems and, as we show in Section 4.4.3, $P = 8.69 \pm 0.05 \text{ d}$ is completely consistent with the orbital period derived from the RV curve. We discuss the nature of the photometric variability in Section 5.4.

4.4.2 NIR spectroscopy

The VLT/SINFONI spectrum of the NIR counterpart to 3XMM J174417.2–293944 has been split into *H*- and *K*-band spectra and plotted in Fig. 9. Similar to IGR J17445–2747, there are a number of strong absorption features present in the NIR spectrum typical of late-type stars (see e.g. Kleinmann & Hall 1986; Wallace & Hinkle 1997; Meyer et al. 1998). We used these features to derive v_{helio} using the IRAF task `rvidlines`. Using only lines in the *H*-band region of the spectrum, we derive $v_{\text{helio}} = 134 \pm 14 \text{ km s}^{-1}$, whereas using

Table 4. Equivalent widths of spectral features in the *K*-band region of the VLT/SINFONI spectrum of the NIR counterpart to 3XMM J174417.2–293944.

Feature	EW (\AA)
Na I	3.33 ± 0.14
Ca I	2.27 ± 0.38
^{12}CO	7.85 ± 0.57

only lines in the *K*-band region of the spectrum, we derive $v_{\text{helio}} = 45 \pm 7 \text{ km s}^{-1}$. Aside from being inconsistent between the two bands, these velocities also differ from the predicted velocity from the optical RV curve presented in the following section. The discrepancy between the *H* and *K* bands suggests a relative wavelength calibration error $\sim 6 \text{ \AA}$, which is approximately twice the expected RMS uncertainty of the wavelength calibration. However, this level of error is not significant enough to prevent line identification or calculation of EWs (the latter has precision that is two orders of magnitude larger than this calibration issue). Therefore we use the derived v_{helio} in each band to act as a re-calibration of the wavelength solution for the purposes of displaying rest-frame spectra in Fig. 9.

Similar to our analysis of IGR J17445–2747, we can apply two-dimensional spectral classification techniques to determine the nature of the NIR counterpart to 3XMM J174417.2–293944. We again adopt the passbands and continua defined in Table 2 to calculate EWs. Uncertainties on EWs were estimated using the ‘bootstrap-with-replacement’ technique described in Section 4.1.3. The calculated EWs are listed in Table 4.

4.4.3 Optical Spectroscopy and Radial Velocities

The average SOAR/Goodman optical spectrum of 3XMM J174417.2–293944 is shown in Fig. 10. As with the NIR spectrum, strong absorption features typical of late-type stars are present. We also note a strong, broad (FWHM $\sim 400 \text{ km s}^{-1}$) $H\alpha$ emission feature, indicating that 3XMM J174417.2–293944 is probably an accreting compact object. The absorption features most likely originate from the binary companion. We used the multiple spectra to perform a RV study of the secondary star and derive the binary parameters.

To estimate RVs, we cross-correlated the spectra with the K giant spectral standard. Given the long period of the binary (see Section 4.4.1 and below), for those epochs where two spectra of 3XMM J174417.2–293944 were obtained, we use the weighted average of the two velocities. The barycentric velocities are given in Table 5. The corresponding dates are given as Barycentric Julian Dates (BJD) on the TDB system (Eastman et al. 2010).

We fit a Keplerian model to these RVs using the custom Markov Chain Monte Carlo sampler *TheJoker* (Price-Whelan et al. 2017). We began with a circular fit, in which the free parameters were the orbital period P_{orb} , epoch of the ascending node T_0 (given as a Barycentric Julian Date), RV semi-amplitude of the secondary K_2 , and systemic velocity γ . The posterior distributions are all close to Gaussian and uncorrelated, with best-fit values: $P_{\text{orb}} = 8.7092 \pm 0.0048 \text{ d}$ (consistent with $P = 8.69 \pm 0.05 \text{ d}$ derived from the optical pho-

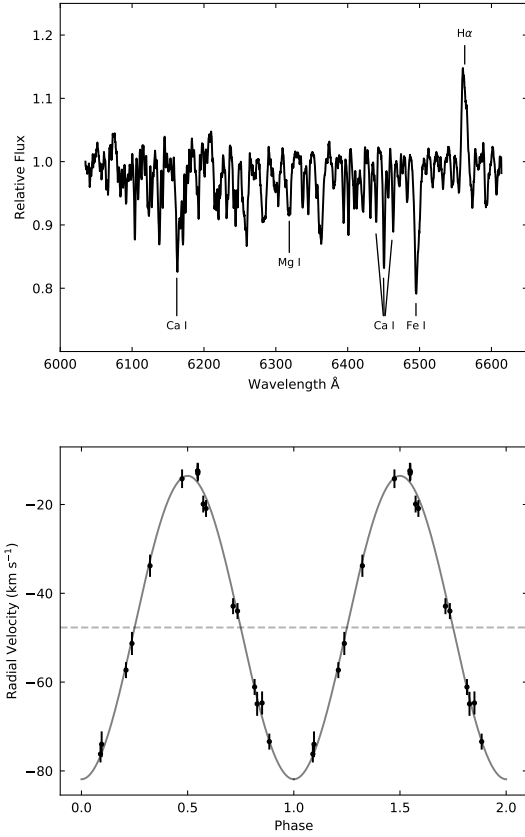


Figure 10. Radial velocity study of the optical counterpart to 3XMM J174417.2–293944. Top: average *SOAR*/Goodman spectrum, continuum normalised. $H\alpha$ is labelled, along with some example absorption features. Bottom: RV curve showing the motion of the secondary star in 3XMM J174417.2–293944, folded on the best-fit $P_{\text{orb}} = 8.7092$ d. The solid curve represents the best-fit Keplerian orbital model, with the parameters derived in the text. The dashed line denotes the systemic velocity of the system $\gamma = -47.7 \pm 0.5 \text{ km s}^{-1}$.

tometry), $T_0 = 2458334.9450 \pm 0.0680$ d, $K_2 = 34.2 \pm 0.7 \text{ km s}^{-1}$, and $\gamma = -47.7 \pm 0.5 \text{ km s}^{-1}$. This fit is good: for the central best-fit values above, the RMS is only 1.8 km s^{-1} , and the χ^2 per degrees of freedom is 14.4/13. The best-fit RV model is shown folded on P_{orb} in Fig. 10.

We also experimented with fits to eccentric orbits: the posterior distribution of the eccentricity had its mode at zero, with a median of $e = 0.03$, and the RMS of this fit was slightly improved at 1.6 km s^{-1} . The period and semi-amplitude of this fit were identical to the circular orbit fit within their uncertainties. Given this marginal evidence for eccentricity, we adopt the circular parameters for the remainder of the paper, but note that a very small eccentricity is possible, and could be constrained with additional RV measurements.

Further inspection of the data suggests a broadening of the absorption line profiles. This is common in close binary systems and is typically due to a spin-up of the star due to tidal synchronization. We used the higher resolution spectra obtained on 2018 Aug 13 (with $R \sim 12000$) to measure $v_r \sin i$, where v_r is the rotational velocity of the compan-

Table 5. Radial velocities obtained from cross-correlation of optical spectra of 3XMM J174417.2–293944 with a K giant spectral standard.

BJD	RV (km s^{-1})
2458202.8039596	-64.9 ± 2.7
2458223.7970651	-51.3 ± 2.6
2458243.9046060	-12.4 ± 1.8
2458243.9145226	-13.0 ± 1.8
2458243.9244391	-12.6 ± 1.9
2458288.9093142	-42.9 ± 1.8
2458289.7916434	-61.1 ± 1.8
2458309.5989186	-76.2 ± 1.9
2458322.5218350	-19.9 ± 1.9
2458344.4821089	-74.0 ± 2.9
2458345.4813442	-57.3 ± 1.8
2458346.4666366	-33.8 ± 2.5
2458356.4906751	-14.2 ± 2.1
2458357.4727641	-20.9 ± 1.9
2458367.4734528	-44.0 ± 1.8
2458368.4812511	-64.7 ± 2.6
2458377.4867468	-73.4 ± 1.8

ion and i is the binary inclination. This was done as described by [Strader et al. \(2014\)](#): we obtained spectra of non-rotating stars of a similar spectral type with the same setup, and then convolved these with kernels reflecting a range of $v_r \sin i$ values with a standard limb-darkening law. Cross-correlation of these convolved spectra with un-broadened spectra then gives a relation between the FWHM of the cross-correlation peak and $v_r \sin i$. Using this method, we find $v_r \sin i = 53.0 \pm 2.0 \text{ km s}^{-1}$.

5 DISCUSSION

5.1 IGR J17445–2747: A bursting neutron star with a giant companion

The *Chandra* position of IGR J17445–2747 contains one extremely bright star, which we have shown has a 0.3 per cent probability to occur by chance alignment, so we take this as the likely stellar counterpart. The faintness of this object in the optical, coupled with its brightness at NIR wavelengths, suggests that the companion is likely a distant, reddened giant star. The statistical uncertainties on the distance from the *Gaia* DR2 data (allowing for $1.1 < d < 7.6$ kpc; [Bailer-Jones et al. 2018](#)) are too large to allow a luminosity estimate sufficiently accurate to distinguish between a dwarf or giant nature, especially given that there is likely to be some substantial accretion light component in the optical bandpass. Table 3 details the EWs of NIR spectral features important for spectral classification. [Comerón et al. \(2004\)](#) show (in their figs. 8–13) that the EW of the ^{12}CO feature is always $> 25 \text{ Å}$ in supergiants. We measure $\text{EW}[^{12}\text{CO}] = 13.50 \pm 0.88 \text{ Å}$, more typical of giants and dwarfs. We can therefore confidently rule out the possibility of a supergiant.

It has been shown that we can separate giants from dwarfs by comparing the EWs of Na I, Ca I and ^{12}CO . [Ramírez et al. \(1997\)](#) demonstrate that $\log\{\text{EW}[^{12}\text{CO}]/(\text{EW}[\text{Na I}] + \text{EW}[\text{Ca I}])\}$ should be in the range -0.22 – 0.06 for dwarfs and 0.37 – 0.61 for giants (see their fig. 11). We measure this quantity to be 0.86 ± 0.23 ,

significantly above the dwarfs and likely indicative of a giant (though not completely consistent within 1σ uncertainties). A bright giant, class II, is also a possibility. A final piece of evidence to support the giant hypothesis lies in fig. 10 of Ramirez et al. (1997), which demonstrates that giants and dwarfs are clearly distinguished in plots of EW[Na I] vs EW[^{12}CO] and EW[Na I + Ca I] vs EW[^{12}CO]. In both cases, the likely counterpart for IGR J17445–2747 lies in the portion of the plots occupied by giants. Ramirez et al. (1997) also define a relationship between EW[^{12}CO] and the effective temperature, T_{eff} for giant stars:

$$T_{\text{eff}} = (5019 \pm 79) - (68 \pm 4) \times \text{EW}[^{12}\text{CO}]. \quad (4)$$

We calculate $T_{\text{eff}} = 4100 \pm 110\text{K}$, propagating the uncertainty in EW[^{12}CO]. The relationship between T_{eff} and spectral type derived for giants by van Belle et al. (1999) indicates that $T_{\text{eff}} = 4100\text{K}$ is consistent with spectral type K4.3, whilst the calibration presented by Richichi et al. (1999) suggests a consistent K4 giant. The calibration presented by Ramirez et al. (1997) suggests K3.6. We therefore adopt a median spectral type of K4III (with a reasonable range of K3–5III; Richichi et al. 1999) for the companion star of IGR J17445–2747. This implies a typical radius of $R_{\star} = 45 \pm 9 R_{\odot}$ (van Belle et al. 1999; see also e.g. Alonso et al. 2000) and therefore an expected luminosity range $L \approx 500 \pm 200 L_{\odot}$.

We can also use the derived spectral type to estimate the distance to the source. K4III stars have a characteristic V-band absolute magnitude $M_V = 0.0$ (Schmidt-Kaler 1982). This is equivalent to $M_K = -3.3$ considering the known intrinsic $(V - K)_{\text{int}}$ colour for a K4III star (e.g. Cox 2000; Kučinskas et al. 2005). The observed and known intrinsic NIR colours allow us to place a reasonable constraint on extinction in the K-band, $A_K \sim 1.2$ (adopting the known conversions between extinction in the V-band, A_V and A_K ; Cardelli et al. 1989). This implies $d \sim 2.3$ kpc (with a scatter of ± 0.6 kpc considering the adopted range of K3–5III), much closer than the minimum $d \gtrsim 5$ kpc derived by Mereminskiy et al. (2017) from a spectral analysis of the X-ray burst, assuming solar abundances), though consistent with the derived *Gaia* DR2 range of $1.1 < d < 7.6$ kpc (Bailer-Jones et al. 2018). However, as we note above, the measured $\log\{\text{EW}[^{12}\text{CO}]/(\text{EW}[\text{Na I}] + \text{EW}[\text{Ca I}])\}$ is significantly above the accepted range for dwarfs, and slightly higher than the giants (Ramirez et al. 1997) raising the possibility that the companion of IGR J17445–2747 is instead a class II bright giant. If this is indeed the case, then from the known absolute magnitude of a K-type class II star (Schmidt-Kaler 1982) we would place IGR J17445–2747 at $d \gtrsim 6$ kpc, in agreement with Mereminskiy et al. (2017).

The strong evidence for a giant companion suggests that IGR J17445–2747 is a symbiotic X-ray binary – a compact object accreting from the wind of a giant donor. Although giants can also experience Roche lobe overflow (e.g. the donor to the BH low-mass X-ray binary GRS 1915+105), the expected mass transfer rates will then be quite large, $\sim 10^{-8} \text{ y}^{-1}$ (Vilhu 2002), and the accretion disc should be rather large, producing long, bright outbursts (Deegan et al. 2009), which do not resemble the observed outbursts from IGR J17445–2747.

If it is a symbiotic X-ray binary, then IGR J17445–2747

would be the only known example of a symbiotic X-ray binary that exhibits X-ray bursts (discovered by Mereminskiy et al. 2017). X-ray bursts are thought to only be produced on NSs with $B < 10^{11}$ G (Bildsten 1998), while NSs in symbiotic X-ray binaries generally have $B \sim 10^{12}$ G, explained by their accreting lifetime being too small to bury their magnetic fields from their high initial fields, as often invoked to explain low fields in LMXBs (Cumming et al. 2001). However, not all NSs are born with high fields; several young NSs in supernova remnants have $B = 10^{10-11}$ G (Gotthelf et al. 2013), and Cir X-1, a young HMXB in a supernova remnant, also shows bursts (Heinz et al. 2013). Thus, we argue that IGR J17445–2747 is likely a symbiotic X-ray binary where the NS was born with an initially low B field. A RV study would allow us to confirm the symbiotic nature, as the known symbiotic X-ray binaries exhibit P_{orb} between hundreds of days and several years (Yungelson et al. 2019).

5.2 Swift J175233.9–290952: An unidentified VFX

Of all the sources followed up at optical and NIR wavelengths in this work, Swift J175233.9–290952 has the most uncertain identification. Photometric studies of the suspected counterpart, VVV J175233.93–90947.66, revealed that (a) it had not brightened significantly ($\Delta H \leq 0.3$, $\Delta J \leq 0.6$; Fig. 4) five days after the X-ray source was discovered by *Swift*, and (b) there was no apparent variability in the VVV source. This has rendered us unable to confirm VVV J175233.93–90947.66 as the true counterpart to Swift J175233.9–290952.

Nevertheless, we obtained NIR spectroscopy of the VVV source as it is the only suspected counterpart bright enough to study, and we are able to present some potential scenarios for the nature of Swift J175233.9–290952. We can also rule out a flaring dwarf nature for the X-ray source as it was X-ray active for 2–3 weeks after the initial detection (Maccarone et al. 2017b; Bahramian et al. 2020, in prep.). X-ray flares from late-type stars are typically \sim minutes to \sim hours in duration (see e.g. Pye et al. 2015).

If the VVV source is the true counterpart to the X-ray source, there are limited possibilities for its nature. The lack of an optical counterpart to Swift J175233.9–290952 suggests that the source is either intrinsically red, or heavily reddened. Examining the *Swift*/XRT X-ray spectrum of the source we measure a neutral hydrogen column density $N_{\text{H}} < 7.2 \times 10^{21} \text{ cm}^{-2}$, which, utilizing the known correlation $N_{\text{H}} = (2.81 \pm 0.13) \times 10^{21} A_V$ (Bahramian et al. 2015), equates to $A_V < 2.56$. The NIR source has an observed NIR colour $J - H = 1.32 \pm 0.13$, which, if we adopt the maximum value of A_V derived from the X-ray spectrum, would imply an intrinsic $(J - H)_{\text{int}} = 1.05 \pm 0.13$ (adopting the known conversions between A_V , A_J and A_H ; Cardelli et al. 1989). This implies that VVV J175233.93–90947.66 is intrinsically quite red.

Could VVV J175233.93–90947.66 be the companion in an X-ray binary? The lack of hydrogen emission lines would be quite unusual for an X-ray binary with a hydrogen-rich accretion disc in quiescence (though some show featureless spectra in outburst, e.g. Shahbaz et al. 1996). One may consider an ultracompact X-ray binary, which would not have H lines. The absolute magnitude of ultracompact X-ray binaries in outburst can be estimated by observations

of ultracompact X-ray binaries in globular clusters to be around $M_B \sim 5 \pm 1$ (Deutsch et al. 2000; Haurberg et al. 2010; Edmonds et al. 2003), consistent with predictions from van Paradijs & McClintock (1994). Transient systems have rarely been detected in quiescence, due to their faintness; D’Avanzo et al. (2009) find one ultracompact with $M_V \sim 13$. For a distance of 8 kpc and $A_V \sim 2$ (see above), these suggest $V \sim 21.5$, $V \sim 30$, or (assuming $(V - K) \sim 0$) $K \sim 19.5$, $K \sim 27.5$ for outburst and quiescence respectively. This is far too faint for VVV J175233.93–90947.66 ($H = 15.1$).

Swift J175233.9–290952 could be a young stellar object (YSO), as these exhibit X-ray emission (Feigelson & Montmerle 1999; Preibisch et al. 2005) are intrinsically red, and are often obscured by the molecular clouds in which they are born. However, NIR spectra of YSOs typically exhibit Br γ and H $_2$ emission in the K-band (Cooper et al. 2013), which is absent from VVV J175233.93–90947.66. Additionally, YSOs typically exhibit excess mid-IR emission (e.g. Koenig & Leisawitz 2014), but Swift J175233.9–290952 is not present in mid-IR survey catalogues such as GLIMPSE.

Swift J175233.9–290952 could be a background Active Galactic Nucleus (AGN). Some blazars (AGN with jets pointed toward us) show weak or no emission lines in their spectra (e.g. Landt et al. 2004), similar to Fig. 5. However, blazars are strong radio sources, and the 10 GHz non-detection of Swift J175233.9–290952, combined with a radio/X-ray luminosity ratio much lower than typical accreting BHs (Tetarenko et al. 2017), provides strong evidence against this hypothesis.

Alternatively, VVV J175233.93–90947.66 may not be associated with Swift J175233.9–290952, considering the stellar crowding in this field. We note that the probability of the *Chandra* position being coincident with a star as bright or brighter than VVV J175233.93–90947.66 is 8 per cent. The first photometric measurements of the field (which found $K > 14.6$) occurred five days after the initial X-ray outburst. The *VLT*/SINFONI observation, which reached a depth of $K \sim 18$, took place more than a month later, at which point the X-ray emission had faded into quiescence (Bahramian et al. 2020, in prep.). As discussed above, an ultracompact X-ray binary outburst (e.g. $L_X \sim 10^{36} \text{ erg s}^{-1}$) would likely reach $K \sim 19 - 20$ (i.e. undetectable in our photometric data), while an outburst from an LMXB with a ~ 2 h orbit (such as SAX J1808.4–3658, Roche et al. 1998, or NGC 6652A, Engel et al. 2012) would likely reach $K \sim 16 - 18$, beyond the limiting magnitude of the GROND images, which were obtained during the outburst of Swift J175233.9–290952. In quiescence, an ultracompact X-ray binary would be quite undetectable, while an LMXB with $P_{\text{orb}} \sim 2$ h like SAX J1808.4–3658 ($M_I = 7.3$, Deloye et al. 2008) would likely be at $K \sim 21 - 22$. Indeed, Fig. 4 shows that there is another, fainter source inside the *Chandra* error circle at $K \sim 18$. This could be the true NIR counterpart of Swift J175233.9–290952, but it is too faint to obtain a useful spectrum with current technology and reasonable exposure times. Should the true counterpart of Swift J175233.9–290952 have a relatively short orbital period, such as the examples discussed above, the quiescent counterpart is likely undetected.

5.3 1SXPS J174215.0–291453: A chromospherically active binary

The optical counterpart of 1SXPS J174215.0–291453 has a known *Gaia* distance ($d = 78.1 \pm 0.3 \text{ pc}$)⁸, allowing us to place it on the H-R diagram. We use the upper limit to N_H from the source’s X-ray spectrum to constrain the extinction to $A_V < 0.08$. Using APASS magnitudes and this extinction, we infer $M_V = 8.28 \pm 0.02$ and an intrinsic $(B - V)_{\text{int}} = 1.40 \pm 0.03$, placing 1SXPS J174215.0–291453 on the main sequence in a *Hipparcos* H-R diagram (Perryman et al. 1997; van Leeuwen 2007, see Fig. 11), classifying the source as a dwarf.

The *SOAR*/Goodman optical spectrum of the counterpart in Fig. 7 exhibits lines typical of late-type stars and allows us to derive the full spectral type. The strong absorption bands in the range $\sim 6100 - 7400 \text{ \AA}$ are due to a combination of CaH, CaOH and TiO, which indicate an M dwarf (e.g. Reid et al. 1995). Comparing the $J - K_s$ and $R - K_s$ colours (Fitzpatrick 1999), from 2MASS and the USNO-B1 catalogue (Monet et al. 2003), indicates an $\lesssim M3V$ star. In §4.3 we derive a flux ratio $R \approx 0.7$ from the TiO 5 bandhead. Utilising the relationship between $R_{\text{TiO}5}$ and spectral type defined by Reid et al. (1995) we find that 1SXPS J174215.0–291453 is of spectral type $M1(\pm 0.5)V$. This classification is supported by other flux ratios such as TiO 2 (7058–7061 \AA) and CaH 3 (6960–6990 \AA).

The presence of narrow Balmer lines in emission indicate that the source is chromospherically active (Reid et al. 1995; Hawley et al. 1996; Alonso-Floriano et al. 2015), explaining the X-ray emission detected in the *Swift* GBS, and by *XMM-Newton*. We measure $L_X(0.2 - 10 \text{ keV}) \sim 2 \times 10^{29} \text{ erg s}^{-1}$ which is within the known luminosity range for M-dwarfs (e.g. Doyle 1989; González-Álvarez et al. 2019). However, the large RV ($v_{\text{helio}} = -104 \pm 2 \text{ km s}^{-1}$) is somewhat puzzling. *Gaia* DR2 measures a proper motion $\mu \approx 46 \text{ mas y}^{-1}$, which translates to a transverse velocity of $\sim 17 \text{ km s}^{-1}$, a normal kinematic value for a disc star. The large RV (compared to the transverse velocity) suggests that 1SXPS J174215.0–291453 is likely a close binary system, with at least one of the components a chromospherically active M-dwarf, and no evidence for accretion.

5.4 3XMM J174417.2–293944: A white dwarf binary with a subgiant companion

The folded ASAS-SN V-band light curve of 3XMM J174417.2–293944 in Fig. 8 shows distinct periodic variability. However, the nature of the variability remains unclear. The light curve in Fig. 8 does not resemble an ellipsoidal light curve, which would have two maxima at phases 0 and 0.5, and two minima at phases 0.25 and 0.75 (as we have defined orbital phase). The variability may be due to starspots (Oláh et al. 2018) rotating with the star, synchronised to P_{orb} (e.g. Thompson et al. 2018).

The *VLT*/SINFONI $H + K$ -band spectrum of the NIR counterpart to 3XMM J174417.2–293944 presented in Fig. 9 enables us to identify the spectral class of the donor, similarly to IGR J17445–2747. We measure $\text{EW}[^{12}\text{CO}] = 7.85 \pm$

⁸ from inverting the measured parallax, which is an acceptable method of deriving d in cases such as this where the fractional parallax uncertainty is small (Luri et al. 2018)

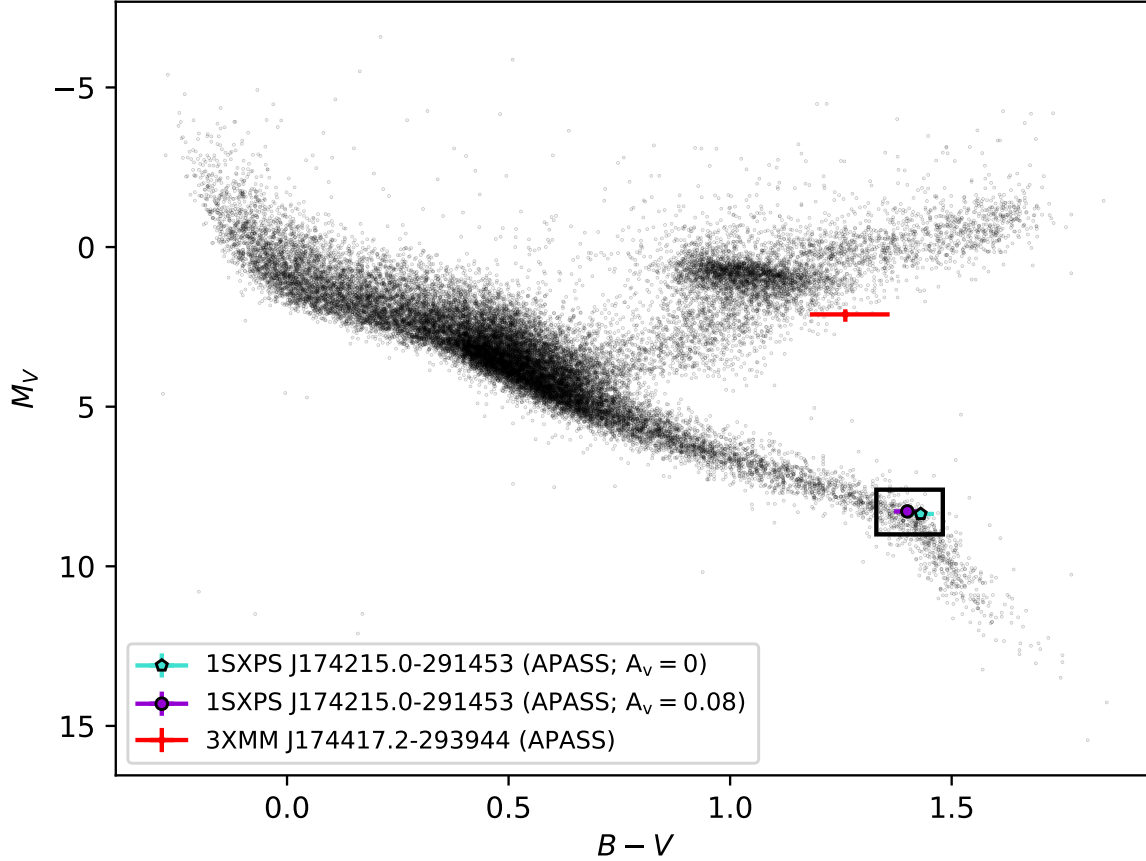


Figure 11. Hertzsprung-Russell diagram constructed from the improved *Hipparcos* catalogue (van Leeuwen 2007). The y-axis denotes the absolute magnitude M_V calculated from the *Hipparcos* parallaxes and the x-axis denotes the $B - V$ colour. The cyan and magenta points (a box is drawn to guide the eye) highlight the location of the optical counterpart to 1SXPS J174215.0–291453 on the main sequence, assuming the minimum ($A_V = 0$) and maximum ($A_V = 0.08$) values for extinction. The red point highlights the optical counterpart to 3XMM J174417.2–293944, corrected for extinction, below the giant branch.

0.57, ruling out a supergiant (Comerón et al. 2004). We measure $\log\{\text{EW}^{[12\text{CO}]} / (\text{EW}[\text{Na I}] + \text{EW}[\text{Ca I}])\} = 0.15 \pm 0.05$, between the typical values for giants and dwarfs derived by Ramírez et al. (1997). Comparing our measured EWs with figs. 9 and 10 and table 5 of Ramírez et al. (1997) does little to resolve the ambiguity, with $\text{EW}^{[12\text{CO}]}$ consistent with those of late-type dwarfs, but the $\text{EW}[\text{Na I}]$ and $\text{EW}[\text{Ca I}]$ are more typical of giants (though a dwarf nature is still possible with these EWs). We therefore suggest that the spectral class of 3XMM J174417.2–293944 lies between a dwarf and a giant, i.e. it may be a subgiant (class IV).

We derive the extinction in the direction of 3XMM J174417.2–293944, $A_V = 1.37^{+0.21}_{-0.13}$ by measuring N_{H} from the best-fit X-ray spectrum and using the Bahramian et al. (2015) A_V – N_{H} correlation. We calculate $M_V = 2.11^{+0.23}_{-0.16}$ and $(B - V)_{\text{int}} = 1.26^{+0.10}_{-0.08}$ using the reported APASS magnitudes and colours and the Gaia distance $d = 990 \pm 40$ pc⁹.

These values place 3XMM J174417.2–293944 below the giant branch on the H-R diagram (Fig. 11).

Assuming that the secondary (the visible star) fills its Roche lobe and that its rotation is synchronized with the orbital period, its projected rotational velocity along our line of sight is given by:

$$v_r \sin i = K_2(1 - e^2)^{1/2} \frac{0.49q^{2/3}(1 + q)}{0.6q^{2/3} + \ln(1 + q^{1/3})}. \quad (5)$$

Here $q = M_2/M_1$ is the mass ratio of the secondary to the primary, and we have used the approximation for the effective radius of the donor Roche lobe from Eggleton (1983), valid for all reasonable q values. Using the posterior samples of K_2 and drawing samples from the observed $v_r \sin i$, we find $q = M_2/M_1 = 2.40 \pm 0.11$. When combined with the mass function of the primary inferred from the K_2 and orbital period, this implies $M_1 \sin^3 i = 0.415 \pm 0.028 M_\odot$. This would make the minimum mass of the observed star (i.e. if $i = 90^\circ$) $M_{2,\text{min}} = 1.0 M_\odot$.

We can draw several conclusions about the nature of the

⁹ from inverting the parallax, again see Luri et al. (2018)

primary. Fitting a single Gaussian to the $H\alpha$ emission line reveals a FWHM $\sim 450 \text{ km s}^{-1}$. LMXBs, particularly those containing BHs and with high accretion rates, typically exhibit FWHM $\gtrsim 1000 \text{ km s}^{-1}$, whereas CVs are seen to exhibit FWHM $\gtrsim 300 \text{ km s}^{-1}$ (see e.g. Casares 2015), so this suggests a white dwarf accretor.

The *XMM-Newton* spectrum shows evidence of emission features at $\sim 1 \text{ keV}$, consistent with the Fe xxiii/xxiv L-shell transition complex (Bahramian et al. 2020, in prep.). Such features are typical of CVs (e.g. Ramsay et al. 2001; Mukai et al. 2003), but have occasionally been seen in NS-LMXBs (e.g. van den Eijnden et al. 2018), so this evidence alone does not rule out a NS primary.

We can examine the companion a number of ways in order to draw more solid conclusions about its evolutionary state. Using an approximation for calculating the stellar effective temperature from $(B - V)_{\text{int}}$ (Sekiguchi & Fukugita 2000; Ballesteros 2012) we find $T_{\text{eff}} \approx 4200 \text{ K}$. (We calculate $T_{\text{eff}} \approx 4500 \text{ K}$ if we assume a giant donor and utilise the relationship between $\text{EW}[^{12}\text{CO}]$ and T_{eff} (Ramirez et al. 1997) and $T_{\text{eff}} \approx 3600 \text{ K}$ assuming a dwarf (Ali et al. 1995). *Gaia* DR2 reports $T_{\text{eff}} = 4019_{-150}^{+188} \text{ K}$.) The donor would be a K3 giant (e.g. van Belle et al. 1999), therefore a slightly later type subgiant. To convert M_V to L_{bol} , we assume an extreme case, for example in the case of a giant star of a similar spectral type, to calculate an upper limit to L_{bol} . Assuming $\text{BC} = -1.02$ (A K5 giant; Cox 2000) we find $L_{\text{bol}} \lesssim 29 L_{\odot}$. This places the companion of 3XMM J174417.2–293944 redward of the post-main-sequence evolutionary tracks of stars no more massive than $2.5 M_{\odot}$ (Schaller et al. 1992), which we adopt as a realistic upper limit to M_2 . This means that $M_1 < 1.04 M_{\odot}$ – the primary is almost certainly a WD. The primary’s maximum mass also allows us to derive a binary inclination $i > 47^\circ$.

The upper limit to L_{bol} combined with the derived T_{eff} allows us to estimate the radius of the companion to be $R_{\star} \lesssim 10 R_{\odot}$. This suggests a subgiant, as giants of similar temperature are typically twice as large in radius (e.g. van Belle et al. 1999; Alonso et al. 2000). We use Kepler’s third law and the derived range of masses for the primary to calculate the binary separation $a \approx 19.8 - 26.9 R_{\odot}$. Following Eggleton (1983) the size of the Roche lobe of the secondary is $R_{\text{RL},2} \approx 9.0 - 12.3 R_{\odot}$. The $R_{\star} \lesssim 10 R_{\odot}$ secondary is therefore consistent with filling, or nearly filling, its Roche lobe.

We can estimate the mass-loss rate of the stellar companion to see whether the source can be powered by accretion of a stellar wind. Using Reimers’ Law (Reimers 1977) and choosing a reasonable range of companion masses, luminosities and radii (see above), we estimate the mass-loss rate from the late-type companion to be $\dot{M}_2 \sim 10^{-11} - 10^{-10} M_{\odot} \text{ y}^{-1}$ (see also Willems & Kolb 2003). Using the standard Bondi-Hoyle-Littleton formalism (Hoyle & Lyttleton 1941; Bondi & Hoyle 1944) to estimate the average mass accretion rate onto the compact object we find $\dot{M}_{\text{acc}} \sim 10^{-13} M_{\odot} \text{ y}^{-1}$ using a median $\dot{M}_2 = 5 \times 10^{-11} M_{\odot} \text{ y}^{-1}$. This translates to an inferred bolometric luminosity $L_{\text{bol}} \sim 6 \times 10^{29} - 3 \times 10^{30} \text{ erg s}^{-1}$ (assuming the known range of masses for the WD primary and the Nauenberg 1972 WD mass-radius relation), well below the measured X-ray luminosity range ($0.3 - 10 \text{ keV}$ $L_X \sim 5 \times 10^{31-33} \text{ erg s}^{-1}$, averaging $L_X \sim 10^{32} \text{ erg s}^{-1}$; Bahramian et al. 2020, in prep.), indicating that spherical accretion of

a stellar wind is not responsible for the observed luminosity of 3XMM J174417.2–293944.

The classic picture of a CV involves a WD accreting matter via Roche-lobe overflow (RLO) from a (less massive) main sequence companion, with typical $P_{\text{orb}} \lesssim 6 \text{ h}$. However, if 3XMM J174417.2–293944 is a RLO system, with $P_{\text{orb}} = 8.7092 \pm 0.0048 \text{ d}$ and $q > 1$, it would have an unusually long period, the longest for any known CV (Ritter & Kolb 2003). Several low-mass X-ray binaries with NSs in this period range are known, where mass transfer is driven by an evolved companion losing mass on the nuclear timescale (Webbink et al. 1983), producing mass transfer rates $\sim 10^{-8} M_{\odot} \text{ y}^{-1}$ (Podsiadlowski et al. 2002). We note that this would give an extremely high accretion luminosity of $L \sim 6 \times 10^{34} - 3 \times 10^{35} \text{ erg s}^{-1}$, which would likely produce an optically thick layer around the CV radiating most of this luminosity in the UV, which is not seen from this source (Rivera Sandoval et al. 2020, in prep.). Even more problematic for this interpretation is that the high mass ratio ($q > 1$, i.e. $M_2 > M_1$) of this object would lead to rapid, thermal timescale mass transfer (Ivanova & Taam 2004), with higher mass transfer rates up to $10^{-6} M_{\odot} \text{ y}^{-1}$ for a few 10^6 years, a large optically thick envelope around the WD, and possibly lead to a Type Ia supernova explosion (Han & Podsiadlowski 2004). The high mass transfer rate in this scenario would lead to a variety of observable effects (supersoft X-rays, strong broad optical emission lines; see e.g. Southwell et al. 1996) that do not match our observations.

Alternatively, the subgiant is close to filling its Roche lobe, and its stellar wind is gravitationally focused in the direction of the WD (Friend & Castor 1982). In a focused wind case, the mass-accretion rate on to the compact object can be up to 5–20 per cent of the total wind mass-loss rate from the donor, much more efficient than the Bondi-Hoyle-Littleton approximation (de Val-Borro et al. 2017). Again adopting the median $\dot{M}_2 = 5 \times 10^{-11} M_{\odot} \text{ y}^{-1}$ we find in the focused wind case an inferred $L_{\text{bol}} \sim 9 \times 10^{30} - 2 \times 10^{32} \text{ erg s}^{-1}$. A focused wind could therefore account for the observed X-ray properties of 3XMM J174417.2–293944. Focused wind accreting binaries can be seen as an evolutionary stage between symbiotic binaries and RLO systems (Friend & Castor 1982). We find the focused-wind scenario the most physically plausible to explain 3XMM J174417.2–293944.

6 CONCLUSIONS

We give results of optical/NIR follow-up of X-ray sources detected in the first year of the Swift Bulge Survey:

- IGR J17445–2747 is a NS binary (known from X-ray bursts) with a giant companion. This is likely to be a symbiotic X-ray binary (i.e. the NS accretes from the giant’s wind), and the first symbiotic X-ray binary showing X-ray bursts, indicating a relatively low B field at birth, since symbiotic X-ray binaries have short lifetimes.
- An unidentified source, Swift J175233.9–290952. The near-IR spectrum of the brightest star within the error circle (VVV J175233.93–90947.66) shows no evidence for accretion, suggesting that the true optical counterpart is relatively faint, and (considering the relation between outburst optical brightness and orbital period) may have a relatively short orbital period.

- 1SXPS J174215.0–291453 is a nearby binary containing at least one chromospherically active M dwarf.

- 3XMM J174417.2–293944 is a WD binary with a sub-giant companion in an 8.7 d orbital period. The companion is more massive than the primary ($q = 2.4 \pm 0.1$). Neither standard Bondi-Hoyle-Littleton accretion from a wind, nor Roche-lobe overflow, account for the physical picture. We argue that the X-ray emission may be driven by a focused wind; in which case this would be the first known system of a WD accreting from its companion's focused wind.

The sources detected in the first year of the SBS that we have obtained significant follow-up observations of all have drastically different natures. It is clear that faint X-ray sources cannot be attributed to one mechanism. However, our in-depth studies of IGR J17445–2747 and 3XMM J174417.2–293944 indicate that binaries with giant companions may contribute significantly to the VFXT population. The SBS commenced its second year of operations in April 2019, and we are proceeding with optical/NIR follow-up of transient X-ray sources to extend our understanding of these sources.

ACKNOWLEDGEMENTS

The authors thank the anonymous referee for useful comments that helped improve the manuscript, and N. Ivanova, K. Van and R. Hatfull for useful discussions on 3XMM J174417.2–293944. AWS thanks R. Plotkin for helpful comments on revising the manuscript.

COH & GRS acknowledge NSERC Discovery Grants RGPIN-2016-04602 and RGPIN-2016-06569 respectively, and COH also a Discovery Accelerator Supplement. TJM and LERS thank NASA for support under grant 80NSSC17K0334. JS acknowledges support from a Packard Fellowship. ND is supported by a Vidi grant from the Netherlands Organisation for Scientific Research (NWO).

Based on observations obtained at the Gemini Observatory (processed using the Gemini IRAF package), which is operated by the Association of Universities for Research in Astronomy, Inc., under a cooperative agreement with the NSF on behalf of the Gemini partnership: the National Science Foundation (United States), National Research Council (Canada), CONICYT (Chile), Ministerio de Ciencia, Tecnología e Innovación Productiva (Argentina), Ministério da Ciência, Tecnologia e Inovação (Brazil), and Korea Astronomy and Space Science Institute (Republic of Korea). The authors also wish to recognize and acknowledge the very significant cultural role and reverence that the summit of Maunakea has always had within the indigenous Hawaiian community. We are most fortunate to have the opportunity to conduct observations from this mountain. Based on observations collected at the European Organisation for Astronomical Research in the Southern Hemisphere under ESO programmes 099.D-0826(C), 099.D-0826(D) and 099.A-9025(A). Part of the funding for GROND (both hardware as well as personnel) was generously granted from the Leibniz-Prize to Prof. G. Hasinger (DFG grant HA 1850/28-1). Based on observations obtained at the Southern Astrophysical Research (SOAR) telescope, which is a joint project of the Ministério da Ciência, Tecnologia, Inovações e Comunicações (MCTIC) do

Brasil, the U.S. National Optical Astronomy Observatory (NOAO), the University of North Carolina at Chapel Hill (UNC), and Michigan State University (MSU). This work has made use of data from the European Space Agency (ESA) mission *Gaia* (<https://www.cosmos.esa.int/gaia>), processed by the *Gaia* Data Processing and Analysis Consortium (DPAC; <https://www.cosmos.esa.int/web/gaia/dpac/consortium>). Funding for the DPAC has been provided by national institutions, in particular the institutions participating in the *Gaia* Multilateral Agreement. This research made use of ASTROPY (<https://www.astropy.org>), a community-developed core PYTHON package for Astronomy (Astropy Collaboration et al. 2013, 2018).

REFERENCES

- Ali B., Carr J. S., Depoy D. L., Frogel J. A., Sellgren K., 1995, *AJ*, **110**, 2415
- Alonso-Floriano F. J., et al., 2015, *A&A*, **577**, A128
- Alonso A., Salaris M., Arribas S., Martínez-Roger C., Asensio Ramos A., 2000, *A&A*, **355**, 1060
- Ambrosino F., et al., 2017, *Nature Astronomy*, **1**, 854
- Armas Padilla M., Degenaar N., Russell D. M., Wijnand s R., 2013, *MNRAS*, **428**, 3083
- Astropy Collaboration et al., 2013, *A&A*, **558**, A33
- Astropy Collaboration et al., 2018, *AJ*, **156**, 123
- Bahramian A., Gladstone J. C., Heinke C. O., Wijnands R., Kaur R., Altamirano D., 2014, *MNRAS*, **441**, 640
- Bahramian A., Heinke C. O., Degenaar N., Chomiuk L., Wijnands R., Strader J., Ho W. C. G., Pooley D., 2015, *MNRAS*, **452**, 3475
- Bahramian A., et al., 2017, *The Astronomer's Telegram*, **10355**
- Bahramian A., et al., 2020, in prep.
- Bailer-Jones C. A. L., Rybizki J., Foesneau M., Mantelet G., Andrae R., 2018, *AJ*, **156**, 58
- Ballesteros F. J., 2012, *EPL (Europhysics Letters)*, **97**, 34008
- Bandyopadhyay R. M., et al., 2005, *MNRAS*, **364**, 1195
- Benjamin R. A., et al., 2003, *PASP*, **115**, 953
- Bertin E., 2006, in Gabriel C., Arviset C., Ponz D., Enrique S., eds, *Astronomical Society of the Pacific Conference Series Vol. 351, Astronomical Data Analysis Software and Systems XV*. p. 112
- Bertin E., Arnouts S., 1996, *A&AS*, **117**, 393
- Bertin E., Mellier Y., Radovich M., Missonnier G., Didelon P., Morin B., 2002, in Bohlender D. A., Durand D., Handley T. H., eds, *Astronomical Society of the Pacific Conference Series Vol. 281, Astronomical Data Analysis Software and Systems XI*. p. 228
- Bildsten L., 1998, in Buccheri R., van Paradijs J., Alpar A., eds, *Vol. 515, NATO Advanced Science Institutes (ASI) Series C*. p. 419 ([arXiv:astro-ph/9709094](https://arxiv.org/abs/astro-ph/9709094))
- Bird A. J., et al., 2006, *ApJ*, **636**, 765
- Bird A. J., et al., 2007, *ApJS*, **170**, 175
- Bird A. J., et al., 2010, *ApJS*, **186**, 1
- Bleach J. N., 2002, *MNRAS*, **332**, 689
- Bogdanov S., et al., 2015, *ApJ*, **806**, 148
- Bondi H., Hoyle F., 1944, *MNRAS*, **104**, 273
- Burrows D. N., et al., 2005, *Space Sci. Rev.*, **120**, 165
- Cardelli J. A., Clayton G. C., Mathis J. S., 1989, *ApJ*, **345**, 245
- Casares J., 2015, *ApJ*, **808**, 80
- Chakrabarty D., Jonker P. G., Markwardt C. B., 2017, *The Astronomer's Telegram*, **10395**
- Chambers K. C., et al., 2016, arXiv e-prints, [p. arXiv:1612.05560](https://arxiv.org/abs/1612.05560)
- Clemens J. C., Crain J. A., Anderson R., 2004, in Moorwood A. F. M., Iye M., eds, *Proc. SPIE Vol. 5492*,

- Ground-based Instrumentation for Astronomy. pp 331–340, doi:10.1117/12.550069
- Comerón F., Torra J., Chiappini C., Figueras F., Ivanov V. D., Ribas S. J., 2004, *A&A*, **425**, 489
- Cooper H. D. B., et al., 2013, *MNRAS*, **430**, 1125
- Coriat M., Fender R. P., Dubus G., 2012, *MNRAS*, **424**, 1991
- Cornelisse R., et al., 2002, *A&A*, **392**, 885
- Corral-Santana J. M., Casares J., Muñoz-Darias T., Rodríguez-Gil P., Shahbaz T., Torres M. A. P., Zurita C., Tyndall A. A., 2013, *Science*, **339**, 1048
- Cox A. N., 2000, Allen’s astrophysical quantities
- Cumming A., Zweibel E., Bildsten L., 2001, *ApJ*, **557**, 958
- D’Avanzo P., Campana S., Casares J., Covino S., Israel G. L., Stella L., 2009, *A&A*, **508**, 297
- DeWitt C., Bandyopadhyay R. M., Eikenberry S. S., Blum R., Olsen K., Sellgren K., Sarajedini A., 2010, *ApJ*, **721**, 1663
- Deegan P., Combet C., Wynn G. A., 2009, *MNRAS*, **400**, 1337
- Degenaar N., Wijnands R., 2009, *A&A*, **495**, 547
- Degenaar N., Wijnands R., 2010, *A&A*, **524**, A69
- Degenaar N., et al., 2010, *MNRAS*, **404**, 1591
- Degenaar N., Wijnands R., Cackett E. M., Homan J., in ’t Zand J. J. M., Kuulkers E., Maccarone T. J., van der Klis M., 2012, *A&A*, **545**, A49
- Deloye C. J., Heinke C. O., Taam R. E., Jonker P. G., 2008, *MNRAS*, **391**, 1619
- Deutsch E. W., Margon B., Anderson S. F., 2000, *ApJ*, **530**, L21
- Doyle J. G., 1989, *A&A*, **218**, 195
- Eastman J., Siverd R., Gaudi B. S., 2010, *PASP*, **122**, 935
- Edmonds P. D., Gilliland R. L., Heinke C. O., Grindlay J. E., 2003, *ApJ*, **596**, 1177
- Eggleton P. P., 1983, *ApJ*, **268**, 368
- Eisenhauer F., et al., 2003, in Iye M., Moorwood A. F. M., eds, Proc. SPIE Vol. 4841, Instrument Design and Performance for Optical/Infrared Ground-based Telescopes. pp 1548–1561 (arXiv:astro-ph/0306191), doi:10.1117/12.459468
- Engel M. C., Heinke C. O., Sivakoff G. R., Elshamouty K. G., Edmonds P. D., 2012, *ApJ*, **747**, 119
- Evans I. N., et al., 2010, *ApJS*, **189**, 37
- Feigelson E. D., Montmerle T., 1999, *ARA&A*, **37**, 363
- Fitzpatrick E. L., 1999, *PASP*, **111**, 63
- Friend D. B., Castor J. I., 1982, *ApJ*, **261**, 293
- Gaia Collaboration et al., 2016, *A&A*, **595**, A1
- Gaia Collaboration et al., 2018, *A&A*, **616**, A1
- González-Álvarez E., et al., 2019, *A&A*, **624**, A27
- Gotthelf E. V., Halpern J. P., Alford J., 2013, *ApJ*, **765**, 58
- Greiner J., et al., 2008, *PASP*, **120**, 405
- Hameury J.-M., Lasota J.-P., 2016, *A&A*, **594**, A87
- Han Z., Podsiadlowski P., 2004, *MNRAS*, **350**, 1301
- Haurberg N. C., Lubell G. M. G., Cohn H. N., Lugger P. M., Anderson J., Cool A. M., Serenelli A. M., 2010, *ApJ*, **722**, 158
- Hawley S. L., Gizis J. E., Reid I. N., 1996, *AJ*, **112**, 2799
- Heinke C. O., Cohn H. N., Lugger P. M., 2009, *ApJ*, **692**, 584
- Heinke C. O., Bahramian A., Degenaar N., Wijnands R., 2015, *MNRAS*, **447**, 3034
- Heinke C. O., et al., 2017, The Astronomer’s Telegram, **10265**
- Heinz S., et al., 2013, *ApJ*, **779**, 171
- Henden A. A., Levine S. E., Terrell D., Smith T. C., Welch D., 2012, Journal of the American Association of Variable Star Observers (JAAVSO), **40**, 430
- Hernández Santisteban J. V., et al., 2019, *MNRAS*, **p. 1939**
- Hoyle F., Lyttleton R. A., 1941, *MNRAS*, **101**, 227
- Illarionov A. F., Sunyaev R. A., 1975, *A&A*, **39**, 185
- Ivanov V. D., Rieke M. J., Engelbracht C. W., Alonso-Herrero A., Rieke G. H., Luhman K. L., 2004, *ApJS*, **151**, 387
- Ivanova N., Taam R. E., 2004, *ApJ*, **601**, 1058
- Kausch, W. et al., 2015, *A&A*, **576**, A78
- King A. R., Wijnands R., 2006, *MNRAS*, **366**, L31
- Kleinmann S. G., Hall D. N. B., 1986, *ApJS*, **62**, 501
- Kneivitt G., Wynn G. A., Vaughan S., Watson M. G., 2014, *MNRAS*, **437**, 3087
- Kochanek C. S., et al., 2017, *PASP*, **129**, 104502
- Koenig X. P., Leisawitz D. T., 2014, *The Astrophysical Journal*, **791**, 131
- Kramida A., Yu. Ralchenko Reader J., and NIST ASD Team 2018, NIST Atomic Spectra Database (ver. 5.6.1), [Online]. Available: <https://physics.nist.gov/asd> [2018, November 14]. National Institute of Standards and Technology, Gaithersburg, MD.
- Krivonos R., Revnivtsev M., Lutovinov A., Sazonov S., Churazov E., Sunyaev R., 2007, *A&A*, **475**, 775
- Krivonos R., Tsygankov S., Revnivtsev M., Grebenev S., Churazov E., Sunyaev R., 2010, *A&A*, **523**, A61
- Kuulkers E., 1998, *New Astron. Rev.*, **42**, 1
- Kučinskas A., Hauschildt P. H., Ludwig H. G., Brott I., Vansévičius V., Lindegren L., Tanabé T., Allard F., 2005, *A&A*, **442**, 281
- Landt H., Padovani P., Perlman E. S., Giommi P., 2004, *MNRAS*, **351**, 83
- Lasota J.-P., 2001, *New Astron. Rev.*, **45**, 449
- Laycock S., Grindlay J., van den Berg M., Zhao P., Hong J., Koenig X., Schlegel E. M., Persson S. E., 2005, *ApJ*, **634**, L53
- Lomb N. R., 1976, *Ap&SS*, **39**, 447
- Luna G. J. M., Sokoloski J. L., Mukai K., Nelson T., 2013, *A&A*, **559**, A6
- Luri X., et al., 2018, preprint, (arXiv:1804.09376)
- Maccarone T. J., Patruno A., 2013, *MNRAS*, **428**, 1335
- Maccarone T. J., et al., 2017a, The Astronomer’s Telegram, **10419**
- Maccarone T. J., et al., 2017b, The Astronomer’s Telegram, **10428**
- Mereminskiy I. A., Grebenev S. A., Sunyaev R. A., 2017, *Astronomy Letters*, **43**, 656
- Meyer M. R., Edwards S., Hinkle K. H., Strom S. E., 1998, *ApJ*, **508**, 397
- Minniti D., et al., 2010, *New Astronomy*, **15**, 433
- Monet D. G., et al., 2003, *AJ*, **125**, 984
- Mukai K., 2017, *PASP*, **129**, 062001
- Mukai K., Kinkhabwala A., Peterson J. R., Kahn S. M., Paerels F., 2003, *ApJ*, **586**, L77
- Mukai K., Orio M., Della Valle M., 2008, *ApJ*, **677**, 1248
- Mukai K., et al., 2016, *MNRAS*, **461**, L1
- Muno M. P., Pfahl E., Baganoff F. K., Brandt W. N., Ghez A., Lu J., Morris M. R., 2005a, *ApJ*, **622**, L113
- Muno M. P., Lu J. R., Baganoff F. K., Brandt W. N., Garmire G. P., Ghez A. M., Hornstein S. D., Morris M. R., 2005b, *ApJ*, **633**, 228
- Nauenberg M., 1972, *ApJ*, **175**, 417
- Oláh K., et al., 2018, *A&A*, **620**, A189
- Papitto A., et al., 2013, *Nature*, **501**, 517
- Perryman M. A. C., et al., 1997, *A&A*, **323**, L49
- Pfahl E., Rappaport S., Podsiadlowski P., 2002, *ApJ*, **571**, L37
- Podsiadlowski P., Rappaport S., Pfahl E. D., 2002, *ApJ*, **565**, 1107
- Preibisch T., et al., 2005, *ApJS*, **160**, 401
- Price-Whelan A. M., Hogg D. W., Foreman-Mackey D., Rix H.-W., 2017, *ApJ*, **837**, 20
- Pye J. P., Rosen S., Fyfe D., Schröder A. C., 2015, *A&A*, **581**, A28
- Ramirez S. V., Depoy D. L., Frogel J. A., Sellgren K., Blum R. D., 1997, *AJ*, **113**, 1411
- Ramsay G., et al., 2001, *A&A*, **365**, L294
- Reid I. N., Hawley S. L., Gizis J. E., 1995, *AJ*, **110**, 1838
- Reimers D., 1977, *A&A*, **61**, 217
- Richichi A., Fabbri L., Ragland S., Scholz M., 1999, *A&A*, **344**, 511
- Ritter H., Kolb U., 2003, *A&A*, **404**, 301
- Rivera Sandoval L. E., et al., 2020, in prep.
- Roche P., Chakrabarty D., Morales-Rueda L., Hynes R., Slivan S. M., Simpson C., Hewett P., 1998, *IAU Circ.*, **6885**, 1

Romanova M. M., Ustyugova G. V., Koldoba A. V., Lovelace R. V. E., 2005, *ApJ*, **635**, L165

Roming P. W. A., et al., 2005, *Space Sci. Rev.*, **120**, 95

Rosen S. R., et al., 2016, *A&A*, **590**, A1

Scargle J. D., 1982, *ApJ*, **263**, 835

Schaller G., Schaerer D., Meynet G., Maeder A., 1992, *A&AS*, **96**, 269

Schmidt-Kaler T., 1982, 4.1.2 Intrinsic colors and visual absolute magnitudes (calibration of the MK system). Springer Berlin Heidelberg, Berlin, Heidelberg, pp 14–24, doi:10.1007/10201975_2, https://doi.org/10.1007/10201975_2

Schwobe A. D., 2018, *A&A*, **619**, A62

Sekiguchi M., Fukugita M., 2000, *AJ*, **120**, 1072

Shahbaz T., Smale A. P., Naylor T., Charles P. A., van Paradijs J., Hassall B. J. M., Callanan P., 1996, *MNRAS*, **282**, 1437

Shahbaz T., Charles P. A., King A. R., 1998, *MNRAS*, **301**, 382

Shappee B. J., et al., 2014, *ApJ*, **788**, 48

Shaw A. W., Heinke C. O., Degenaar N., Wijnands R., Kaur R., Forestell L. M., 2017a, *MNRAS*, **471**, 2508

Shaw A. W., et al., 2017b, The Astronomer’s Telegram, **10305**

Shaw A. W., Heinke C. O., Steiner A. W., Campana S., Cohn H. N., Ho W. C. G., Lugger P. M., Servillat M., 2018, *MNRAS*, **476**, 4713

Skrutskie M. F., et al., 2006, *AJ*, **131**, 1163

Smette A., et al., 2015, *A&A*, **576**

Southwell K. A., Livio M., Charles P. A., O’Donoghue D., Sutherland W. J., 1996, *ApJ*, **470**, 1065

Stetson P. B., 1987, *PASP*, **99**, 191

Strader J., Chomiuk L., Sonbas E., Sokolovsky K., Sand D. J., Moskvitin A. e. S., Cheung C. C., 2014, *ApJ*, **788**, L27

Tetarenko B. E., Sivakoff G. R., Heinke C. O., Gladstone J. C., 2016, *ApJS*, **222**, 15

Tetarenko A., et al., 2017, The Astronomer’s Telegram, **10422**, 1

Thompson T. A., et al., 2018, arXiv e-prints, p. arXiv:1806.02751

Tody D., 1986, in Crawford D. L., ed., Society of Photo-Optical Instrumentation Engineers (SPIE) Conference Series Vol. 627, Instrumentation in astronomy VI. p. 733

Tucker M. A., et al., 2018, *ApJ*, **867**, L9

Vilhu O., 2002, *A&A*, **388**, 936

Wallace L., Hinkle K., 1997, The Astrophysical Journal Supplement Series, **111**, 445

Wallace L., Meyer M. R., Hinkle K., Edwards S., 2000, *ApJ*, **535**, 325

Webbink R. F., Rappaport S., Savonije G. J., 1983, *ApJ*, **270**, 678

Weisskopf M. C., Tananbaum H. D., Van Speybroeck L. P., O’Dell S. L., 2000, in Truemper J. E., Aschenbach B., eds, Society of Photo-Optical Instrumentation Engineers (SPIE) Conference Series Vol. 4012, X-Ray Optics, Instruments, and Missions III. pp 2–16 (arXiv:astro-ph/0004127), doi:10.1117/12.391545

Wijnands R., et al., 2006, *A&A*, **449**, 1117

Willems B., Kolb U., 2003, *MNRAS*, **343**, 949

Winkler C., et al., 2003, *A&A*, **411**, L1

Yungelson L. R., Kuranov A. G., Postnov K. A., 2019, *MNRAS*, **485**, 851

Zurita C., et al., 2006, *ApJ*, **644**, 432

de Martino D., et al., 2013, *A&A*, **550**, A89

de Val-Borro M., Karovska M., Sasselov D. D., Stone J. M., 2017, *MNRAS*, **468**, 3408

in ’t Zand J. J. M., Heise J., Muller J. M., Bazzano A., Cocchi M., Natalucci L., Ubertini P., 1999, *Nuclear Physics B Proceedings Supplements*, **69**, 228

in ’t Zand J. J. M., Cornelisse R., Méndez M., 2005, *A&A*, **440**, 287

van Belle G. T., et al., 1999, *AJ*, **117**, 521

van Leeuwen F., 2007, *A&A*, **474**, 653

van Paradijs J., McClintock J. E., 1994, *A&A*, **290**

van den Eijnden J., et al., 2018, *MNRAS*, **475**, 2027

APPENDIX A: FOLLOW-UP TARGETS

IGR J17445–2747 was discovered by the *International Gamma-Ray Astrophysics Laboratory* (*INTEGRAL*; Winkler et al. 2003) and catalogued as an unidentified, variable source (Bird et al. 2006, 2007, 2010; Krivonos et al. 2007, 2010). *Swift*/XRT detected activity from IGR J17445–2747 during the first epoch of the SBS on 2017 April 13 (Heinke et al. 2017). Three days prior to the *Swift*/XRT detection, *INTEGRAL* had detected a thermonuclear burst from the source, identifying the compact object as a NS (Mereminskiy et al. 2017). Analysis of the X-ray burst by Mereminskiy et al. (2017) implied a minimum distance to the source $d \gtrsim 5$ kpc. A short (~ 1 ks) *Chandra* X-ray Observatory (Weisskopf et al. 2000) observation of the source in quiescence allowed precise localisation (Chakrabarty et al. 2017). The X-ray position matches a bright ($K_s = 9.65 \pm 0.06$) source in multiple NIR catalogues, including the 2MASS catalogue (2MASS J17443041–2746004) and the mid-IR Galactic Legacy Infrared Mid-Plane Survey Extraordinaire (GLIMPSE; Benjamin et al. 2003). It also matches a faint, red optical source in the *Panoramic Survey Telescope and Rapid Response System* (*Pan-STARRS*) survey ($i = 19.38 \pm 0.01$; Chambers et al. 2016), but is not detected in filters bluer than i . gives the distance of the optical counterpart (*Gaia* DR2 4060626256817246720) as $1.1 < d < 7.6$ kpc (Bailer-Jones et al. 2018).

Swift J175233.9–290952 was discovered on 2017 May 4 in epoch 3 of the SBS. Follow-up with *Chandra* on 2017 May 25 provided an accurate position (Maccarone et al. 2017b). The X-ray position is consistent with a NIR source in the *Visible and Infrared Survey Telescope for Astronomy* (*VISTA*) Variable in the Via Lactea Survey (VVV; Minniti et al. 2010) catalogue, VVV J175233.93–90947.66. There are no optical or mid-IR catalogued sources here. Follow-up radio observations with the *Karl G. Jansky Very Large Array* (VLA) on 2017 May 13 did not detect a counterpart, with a 3σ upper limit to the luminosity $L_{10\text{GHz}} \lesssim 1.8 \times 10^{26} (d/8\text{ kpc})^2 \text{ erg s}^{-1}$ (Tetarenko et al. 2017).

On 2017 May 19 (epoch 4 of the SBS) we detected activity from a source at the position of the unidentified X-ray source **1SXPS J174215.0–291453** (Maccarone et al. 2017a), and the *XMM-Newton* source 3XMM J174214.9–291459 (Rosen et al. 2016). The *XMM-Newton* position is consistent with a bright source in optical (*Gaia* DR2 4057126472597377152) and NIR (2MASS J17421498–2914590) catalogues, at a distance of $77.6 < d < 78.2$ pc (Bailer-Jones et al. 2018).

On 2017 September 21 (epoch 13 of the SBS) we detected an X-ray source at the position of the *XMM-Newton* source **3XMM J174417.2–293944** (= CXO J174417.2–293943 from the *Chandra* source catalogue; Evans et al. 2010; Bahramian et al. 2020, in prep.). The X-ray position is consistent with a bright source in optical (*Gaia* DR2 4057051396569058432) and NIR (2MASS 17441724–2939444) catalogues, at a *Gaia* distance of $929 < d < 1006$ pc (Bailer-Jones et al. 2018).

This paper has been typeset from a \LaTeX file prepared by the author.